

Spin decomposition and topological properties in a generic electromagnetic field

Peng Shi*, Aiping Yang, Xiaojin Yin, Xinrui Lei, Luping Du*, Xiaocong Yuan*

Nanophotonics Research Centre, Shenzhen Key Laboratory of Micro-Scale Optical Information Technology, Institute of Micro/Nano Optoelectronics, Shenzhen University, 518060, China

* Authors to whom correspondence should be addressed: pittshiustc@gmail.com, lpdu@szu.edu.cn, and xcyuan@szu.edu.cn

Abstract: Electromagnetic spins, including longitudinal and transverse ones, have been playing important roles in light-matter interactions. Here, we formulate a unified equation to uncover the physical origins and topological properties of longitudinal and transverse spins in a generic electromagnetic field. The equation reveals universally that the transverse spin is locked with the kinetic momentum and originated from the transverse inhomogeneities of field, whereas the helix-dependent longitudinal spin orients parallel to the local wavevector. Remarkably, a hidden extraordinary helix-dependent transverse spin possessing helix-dependent spin-momentum locking is discovered and the number of locking states consistent with the nontrivial topological spin Chern number. Furthermore, this spin which determines the inverted helical components is related to the Berry curvature closely. The findings, which are demonstrated experimentally by measuring the three-dimensional spin components in the focusing configuration, will deepen the understanding the underlying physics of spins and open an avenue for chiral quantum optical applications.

Introduction: Spin angular momentum (SAM) is a fundamental dynamical property of elementary particles and classical wave fields [1-9], which plays a critical role in understanding and predicting the behaviors in wave-matter interactions. For a classical electromagnetic (EM) field, SAM in associated with the circular polarizations of electric and magnetic fields can be oriented in an arbitrary direction. It was widely accepted that, for a plane wave solution of Maxwell's equations, the SAM component oriented along its propagating direction (mean wavevector $\hat{\mathbf{k}}$) and helix-dependent (σ) is considered as the longitudinal spin (L-spin) [2], whereas the transverse spin (T-spin) representing the helix-independent SAM components orients perpendicular to the mean wavevector [2,10]. Till now, the T-spin has been investigated in various fields, including Gaussian focused fields [10,11], interference fields [12], evanescent modes [13,14], guided wave modes [15], unpolarized fields [16] and photonic chiral spin textures [17-24]. EM spins can interact intensely with orbital angular momentum (AM), especially in the subwavelength scale, leading to the appearance of research interests in spin-orbit interaction (SOI) [2,25] and many fantastic phenomena, offering potential applications in the fields of optical manipulation [26-28], unidirectional guided wave [29-32], imaging [33-35], communications [36], detection [37], metrology [38] and on-chip quantum technologies [39].

However, if the complicated structured properties [40-42], including the structures/inhomogeneities of intensity, phase, polarization and helix, are introduced into the EM field, it will face physical challenge in distinguishing between L-spin and T-spin with mean wavevector empirically (i.e., longitudinal is parallel to

the mean wavevector while transverse is perpendicular to the mean wavevector). From the physical point of view, a class of physical quantity should possess a unified physical mechanism, yielding a universal equation. In quantum physics, spin is an intrinsic property for elementary particles [43]. In our work, we extract the L-spin correspondence with the concept in quantum physics. On the other hand, the physical origins of T-spin for a generic EM field and its properties are still waited for uncovering quantificationally although most researchers realized that the T-spin will appear in a structured light field.

Here, we formulate a pair of equations to perform the decomposition of the spin vector for a generic EM field, no matter whether in the near-field or in the free space, into the L-spins and T-spins and to uncover their physical origins and accompanied intrinsic topological properties. The decomposition technique is consistent with the Helmholtz decomposition of an arbitrary vector field, and the equations definitely reveal that the L-spin is associated with the EM helix and oriented parallel to the local wavevector while the T-spin is stemmed from the transverse inhomogeneities of an EM field and possesses the property of spin-momentum locking. It is the first time demonstrated that the T-spin in free space possesses the property of spin-momentum locking, which has potential applications in the construction of novel optical spin based chiral topological solitons [17-24] and the chiral manipulation and sorting with the unidirectional optical force [44,45]. Remarkably, if the helical inhomogeneity is introduced to the structured EM field, an extraordinary helix-dependent T-spin will be present and leads to a helix-dependent spin-momentum locking property concurrently. This helix-dependent spin-momentum locking property is consistent with the nontrivial topological spin Chern number of EM field. Moreover, counter-intuitively, this physical differences between the L-spin and T-spin uncovered here would result in the T-spin oriented parallel to the mean wavevector and possessing the property of spin-momentum locking, whereas on the contrary, extraordinary L-spins oriented perpendicular to the mean wavevector and do not possess the property of spin-momentum locking. More interestingly, this helix-dependent T-spin determines the inverted helical component in the EM system and thus it is related to the Berry curvature and evolution of geometric phase in optical system closely. We further demonstrate the helix-dependent properties of T-spins and spin-momentum locking experimentally, by mapping the three components of SAM in a focused beam with circular polarizations in our in-house developed near field imaging system. Our findings could be important for understanding the physical properties of EM spin with potential applications including optical manipulation, robust chiral optical devices and on-chip quantum technologies.

Results: In quantum physics, photons are the spin-1 bosons with the direction of spin parallel to that of photon momentum. For a classical EM field, assuming an elliptically polarized plane light propagating in the p -direction with the electric/magnetic field $\mathbf{E}(\mathbf{r}) = (0\hat{\mathbf{p}} + A_s\hat{\mathbf{s}} + A_p\hat{\mathbf{z}})e^{i(kp-\omega t)}$ and $\mathbf{H}(\mathbf{r}) = (0\hat{\mathbf{p}} - A_p\hat{\mathbf{s}} + A_s\hat{\mathbf{z}})e^{i(kp-\omega t)}/\eta$ in an arbitrary orthogonal coordinate (p, s, z) (see [Supplemental Text II](#)), the total SAM of this elliptically polarized plane light is calculated as $\mathbf{S} = \hbar\sigma\hat{\mathbf{k}}$ with the helix of a single wave-packet $\sigma = \text{Im}\{A_s^*A_p - A_p^*A_s\}/\{A_s^*A_s + A_p^*A_p\}$ (i.e. ratio of the polarization ellipticity to the energy density) [12] and the unit directional vector of local wavevector $\hat{\mathbf{k}}$. Here, the propagating direction associated with the local wavevector is naturally determined by the canonical momentum $\mathbf{P} = \langle\psi|\hat{\mathbf{P}}|\psi\rangle/\hbar\omega$ as $\bar{\mathbf{k}} = \mathbf{P}/\hbar$ with the unit directional vector $\hat{\mathbf{k}} = \bar{\mathbf{k}}/|\bar{\mathbf{k}}|$ and modulus $k = |\bar{\mathbf{k}}|$, $\hat{\mathbf{P}}$ representing the momentum operator in quantum physics [46], $|\psi\rangle$ denoting the classical photon wave function analogous to quantum wave function [47], ω the angular frequency, $\eta = \sqrt{\mu/\epsilon}$ the wave impedance, \hbar the reduced Plank constant. It is worth noting that the special cases of $\sigma=\pm 1$ representing the two circularly polarized plane lights (CPLs) are corresponding to the two helical states in quantum physics [2,24,25]. Thus, the expression of SAM can delineate the globally property of EM field from the perspective of classical theory

as well as the elementary dynamical property of an optical wave-packet from the point of quantum theory. It can be observed that the spin vector of CPL is parallel to the local wavevector $\hat{\mathbf{k}}$ and thus this spin is regarded as L-spin previously. In physics, to keep the theory consistent, the elementary feature of the L-spin in a generic EM field should always coincide with the definition of photonic spin in quantum physics, i.e., the L-spin is parallel to the local wavevector $\hat{\mathbf{k}}$ and its intensity is determined by EM helix σ .

On the other hand, to uncover the physical origin of T-spin, we consider a classical hydrodynamic model where a particle immersed in a fluid possessing a gradient velocity field. Assuming the fluid flows in the $+x$ -direction with its velocity increasing in the y -direction, the immersed particle will suffer a clockwise transverse torque ($-z$ -direction) with its intensity proportional to the local gradient of velocity in the y -direction, whereas if the fluid flows in the $+y$ -direction with its velocity increases in the $+x$ -direction, the immersed particle will suffer an anticlockwise transverse torque ($+z$ -direction) with its intensity proportional to the local gradient of velocity in the $+x$ -direction. In sum, a particle immersed in a fluid flow with gradient velocity will suffer a transverse torque and the intensity of torque is proportional to the vorticity of velocity of fluid flow. Correspondingly, the generation of T-spin in an EM system would be related to the vorticity of photons flow. In the classical EM theory, the energy flow of photons given by the Poynting vector determines the kinetic-Abraham-Poynting momentum $\mathbf{\Pi}$ of photons [48], which can be decomposed into the canonical momentum \mathbf{P} and Belinfante spin momentum $\mathbf{P}_s = \nabla \times \mathbf{S}/2$ ([Supplemental Text I](#)). Thus, these three momenta describing the photons' flow can be regarded as the candidates to evaluate the T-spin. Previously, for a plane wave system, only the canonical momentum associated with the local wavevector was employed to extract the T-spin empirically [2,10]. However, for a generic EM field, it will face basic physical challenges since it cannot uncover the underlying physical difference between the L-spin and T-spin, since the spin momentum \mathbf{P}_s also plays a critical role in the generation of T-spin. Considering a plane EM field with pure L-spin ($\mathbf{S} \propto \hat{\mathbf{k}}$), one can reach easily that the spin momentum $\mathbf{P}_s = \nabla \times \mathbf{S}/2$ is perpendicular to the propagating direction $\hat{\mathbf{k}}$, which is illogical obviously since the \mathbf{P}_s should be parallel to canonical momentum \mathbf{P} in the case. Thus, the spin momentum vanishes for an EM field with pure L-spin, whereas on the contrary, the spin momentum appears as the T-spin is present. On the other hand, for a structured EM field, the canonical group velocity determined by the canonical momentum \mathbf{P} would be superluminal, which contradicts the relativity, and thus the spin momentum appears and is antiparallel to the canonical momentum, which causes the total group velocity associated with the kinetic momentum subluminal [49]. Thus, only the kinetic momentum $\mathbf{\Pi}$ is meaningful in characterizing the flow of photons and will be employed to evaluate the T-spin.

Here, we consider a generic EM field where the electric and magnetic field components can be expanded into the superposition of plane wave basis from the superposition theory of states [50]. To identify the physical reasonability of decomposition of total spin vector into the L-spin and T-spin, we mainly exhibit the results derived from the two-waves interference. Noteworthily, the results can be extended to the multiply-waves interference and thus an arbitrary light field. From the detailed derivations and analysis (see [Supplemental Texts II-V for the proofs](#)), we prove theoretically that the T-spin (\mathbf{S}_t) and L-spin (\mathbf{S}_l) of an arbitrary EM wave can be expressed as

$$\mathbf{S}_t = \frac{1}{2k^2} \nabla \times \mathbf{\Pi}, \quad (1)$$

and

$$\mathbf{S}_l = \hbar \sigma \otimes \hat{\mathbf{k}}. \quad (2)$$

The total spin is given by $\mathbf{S} = \mathbf{S}_l + \mathbf{S}_t = \langle \psi | \hat{\mathbf{S}} | \psi \rangle / \hbar \omega$ with the $\hat{\mathbf{S}}$ representing the spin-1 matrix in SO(3) [47]. The equation (1) definitely reveals that, for an arbitrary EM wave, the T-spin comes from the transverse inhomogeneities of EM field and its transversality constraint satisfies since there is $\nabla \cdot (\nabla \times \mathbf{A}) = 0$ for an arbitrary vector \mathbf{A} . Moreover, the T-spin possesses a widespread property of spin-momentum locking [13], which does not relate to L-spin of EM wave propagating in a homogeneous medium. In unison, the spin-momentum locking originated from the intrinsic spin-orbit coupling in Maxwell's equations is considered as a fundamental property of T-spin for an arbitrary EM field, no matter whether the propagating waves or the evanescent waves. On the other hand, equation (2) clearly represents that the L-spin is determined by the EM helix solely. However, it is worth noting that the L-spin is based on the interlink (given by the self-defined symbol \otimes) between the EM helices of individual waves and their local wavevectors $\hat{\mathbf{k}}$, rather than the mean wavevector. Naturally, in our work, the mean wavevector is given by the canonical momentum of the global EM field while the local wavevector is identified by the canonical momentum of the individual plane wave by expanding the global EM field into the superposition of plane wave basis. Remarkably, since the local wavevector $\hat{\mathbf{k}}$ is proportional to canonical momentum given by the inner product of momentum operator $\hat{\mathbf{P}} = -i\hbar\nabla$ [46] and $\nabla \times \nabla\psi = 0$ for an arbitrary scalar ψ , the decomposition of spin vector into L-spin and T-spin is approximatively similar to the Helmholtz decomposition of an arbitrary vector [50], which makes the concepts of the longitudinal nature and transversality consistent with other physical systems. This consistency is the fundamental starting point of our research.

To detailly explain the L-spin and the relationship between the transverse inhomogeneities of EM field and T-spin, we exhibit several typical examples. First, for an elliptically polarized plane light propagating in p -direction, the amplitude and polarization ellipticity are homogeneous in the whole space. Thus, in the case, there are $\mathbf{S} = \mathbf{S}_l = \hbar\sigma\hat{\mathbf{k}}$ and $\mathbf{S}_t = \nabla \times \mathbf{H}/2k^2 = 0$. Second, for a single polarized evanescent plane wave (such as the transverse magnetic mode: surface plasmon polariton at air/metal interface [51] or the transverse electric mode: Bloch surface wave at multilayered system [52]), there are amplitude inhomogeneity in pz -plane, which leads to a pure T-spin property of field: $\mathbf{S} = \mathbf{S}_t = \nabla \times \mathbf{H}/2k^2 = \hbar(\kappa/k_p)(W/\hbar\omega\hat{\mathbf{s}})$ and $\mathbf{S}_l = 0$, where W is the energy density of evanescent wave, k_p is the propagation constant and $i\kappa$ is the out-of-plane wavevector. In the case, the T-spin is helix-independent, which coincides with the conservation property of angular momentum since the helix cannot be produced apropos of nothing if there is no external source (uniaxial crystal/chiral material) exist. Remarkably, the curl relationship between the SAM and momentum also implies the intrinsic spin-momentum locking property originated from the intrinsic spin-orbit property of Maxwell's equations [13,14,53], i.e., as the propagating direction is inverted, the direction and intensity of the corresponding T-spin is also reversal. Thirdly, for an elliptically polarized evanescent plane waves as shown in Fig. 1 with electric field $\mathbf{E} = (-A_p i\kappa/k \hat{\mathbf{p}} + A_s \hat{\mathbf{s}} + A_p k_p/k \hat{\mathbf{z}})e^{i(k_p p - \kappa z)}$ and magnetic field $\mathbf{H} = (-A_s i\kappa/k \hat{\mathbf{p}} - A_p \hat{\mathbf{s}} + A_s k_p/k \hat{\mathbf{z}})e^{i(k_p p - \kappa z)}/\eta$, the total SAM can be calculated as $\mathbf{S} = \hbar(k^2\sigma/k_p^2)\hat{\mathbf{k}} - W\kappa/\omega k_p \hat{\mathbf{s}}$ (Supplemental Text III). It can be observed that the s -component SAM is corresponding to the helix-independent T-spin of the single polarized evanescent plane wave case and is perpendicular to the local wavevector $\hat{\mathbf{k}}$. However, comparing to the EM helix of the propagating elliptically polarized plane wave, the longitudinal SAM component parallel to local wavevector here contains an additional factor k^2/k_p^2 , which is illogical in physics since the elementary feature of L-spin for a single wave-packet should be constant, although the total AM is not conservative in the system due to the breaking of rotational symmetry [49]. On the other hand, owing to the evanescent property of wave in the z -direction, one can find that there are two types of inhomogeneities here: the intensity inhomogeneity in pz -plane normal to s -axis and the inhomogeneity of helical density in the sz -plane normal to p -axis (the helical density given by the product of amplitude and helix). Thus, one can expect that the T-spin has two components:

$$\mathbf{S}_t = \frac{1}{2k^2} \nabla \times \mathbf{\Pi} = -\hbar \frac{\kappa^2}{k_p^2} \sigma \hat{\mathbf{k}} - \frac{W}{\omega} \frac{\kappa}{k_p} \hat{\mathbf{s}}. \quad (3)$$

Remarkably, the L-spin calculated by subtracting T-spin from the total spin is $\mathbf{S}_l = \mathbf{S} - \mathbf{S}_t = \hbar \sigma \hat{\mathbf{k}}$, which coincides with that of propagating elliptically polarized plane wave. In this way, besides the helix-independent T-spin component, a hidden extraordinary T-spin that is helix-dependent is discovered and validated theoretically. Furthermore, Eq. 3 also indicates the spin-momentum locking property of evanescent plane wave, which reveals that there are four spin-momentum locked states for a generic EM field as shown in Fig. 1. This is consistent with the photonic spin Chern number of EM wave and indicates the photons possess $\mathbb{Z}4$ topological invariance ([Supplemental Text VII](#)). Noteworthily, in the case that the dual symmetry between the electric and magnetic features is broken [13] and there is only a single polarized state survive, the four spin-momentum locked states would be degraded into the two helix-independent states, which coincides with the spin-momentum locking caused by helix-independent T-spin [14].

The aforementioned concepts of EM spin can be generalized to an arbitrary EM wave field, no matter whether at the interface or in the free space, by expanding it into the superpositions of plane wave basis from the principle of the superposition of states [50]. We take the interferential evanescent plane waves in Fig. 2(a) for example here. Here, for the sake of simplicity, we only introduce the two-waves interference since the multiple wave interference takes the same rules. Assuming that the interferential field between the wave 1 obtained by rotating an elliptically polarized evanescent plane wave ($\mathbf{E}_1(\mathbf{r}) = (-A_{p1} i\kappa/k \hat{\mathbf{p}} + A_{s1} \hat{\mathbf{s}} + A_{p1} k_p/k \hat{\mathbf{z}}) e^{i(k_p p - \kappa z)}$) by an angle $+\theta$ and the individual wave 2 obtained by rotating an elliptically polarized evanescent plane wave ($\mathbf{E}_2(\mathbf{r}) = (-A_{p2} i\kappa/k \hat{\mathbf{p}} + A_{s2} \hat{\mathbf{s}} + A_{p2} k_p/k \hat{\mathbf{z}}) e^{i(k_p p - \kappa z)}$) by an angle $-\theta$, the electric field components can be expressed as ([Supplemental Text IV](#))

$$\mathbf{E} = \hat{R}_z(-\theta) \mathbf{E}_1 \left[\hat{R}_z(\theta) \mathbf{r} \right] + \hat{R}_z(\theta) \mathbf{E}_2 \left[\hat{R}_z(-\theta) \mathbf{r} \right], \quad (4)$$

and the magnetic fields can be calculated by the Faraday's law of electromagnetic induction $\mathbf{H} = \nabla \times \mathbf{E} / i\omega\mu$. Here, $\hat{R}_z(\theta)$ is the rotational operator with respect to the z -axis. One can calculate that the energy density contains three parts $W = W_1 + W_2 + W_c$: the energy density of wave 1 $W_1 = \varepsilon k_p^2 (A_{p1}^* A_{p1} + A_{s1}^* A_{s1}) e^{-2\kappa z} / 2k^2$, the energy density of wave 2 $W_2 = \varepsilon k_p^2 (A_{p2}^* A_{p2} + A_{s2}^* A_{s2}) e^{-2\kappa z} / 2k^2$ and the crossed energy density $W_c = \varepsilon k_p^2 \{ (A_{p1}^* A_{p2} e^{-2ik_{s1}s} + A_{p1} A_{p2}^* e^{+2ik_{s1}s}) + (A_{s1}^* A_{s2} e^{-2ik_{s1}s} + A_{s1} A_{s2}^* e^{+2ik_{s1}s}) \} e^{-2\kappa z} / 2k^2$, where $k_{s1} = k_p \sin\theta$, $k_{p1} = k_p \cos\theta$. It can be observed that W_c is local and its integration on the whole plane vanishes. Based on the decomposition of energy density, the mean wavevector of total EM field can be also decomposed into $\hat{\mathbf{k}} = \hat{\mathbf{k}}_1 + \hat{\mathbf{k}}_2 + \hat{\mathbf{k}}_c$: the local wavevector of wave 1 $\hat{\mathbf{k}}_1 = W_1 / \hbar\omega (k_{p1}/k_p \hat{\mathbf{p}} + k_{s1}/k_p \hat{\mathbf{s}} + 0\hat{\mathbf{z}})$, the local wavevector of wave 2 $\hat{\mathbf{k}}_2 = W_2 / \hbar\omega (k_{p1}/k_p \hat{\mathbf{p}} - k_{s1}/k_p \hat{\mathbf{s}} + 0\hat{\mathbf{z}})$, and the crossed wavevector $\hat{\mathbf{k}}_c = W_c / \hbar\omega (k_{p1}/k_p \hat{\mathbf{p}} + 0\hat{\mathbf{s}} + 0\hat{\mathbf{z}})$. Here, $\hat{\mathbf{k}}_c$ represents the local wavevector of the crossed energy density by comparing the total energy density and the mean wavevector of the total interferential fields. In the way, the L-spin can be calculated as: $\mathbf{S}_l = \hbar \sigma_1 \hat{\mathbf{k}}_1 + \hbar \sigma_2 \hat{\mathbf{k}}_2 + \hbar \sigma_c \hat{\mathbf{k}}_c$, where the three helices are

$$\sigma_1 = \frac{\text{Im} \{ A_{s1}^* A_{p1} - A_{s1} A_{p1}^* \}}{A_{p1}^* A_{p1} + A_{s1}^* A_{s1}}, \quad (5)$$

$$\sigma_2 = \frac{\text{Im} \{ A_{s2}^* A_{p2} - A_{s2} A_{p2}^* \}}{A_{p2}^* A_{p2} + A_{s2}^* A_{s2}}, \quad (6)$$

and

$$\sigma_c = \frac{\text{Im} \left\{ \left(A_{s1}^* A_{p2} e^{-2ik_{s1}s} - A_{s1} A_{p2}^* e^{+2ik_{s1}s} \right) + \left(A_{s2}^* A_{p1} e^{+2ik_{s1}s} - A_{s2} A_{p1}^* e^{-2ik_{s1}s} \right) \right\}}{\left(A_{p1}^* A_{p2} e^{-2ik_{s1}s} + A_{p2}^* A_{p1} e^{+2ik_{s1}s} \right) + \left(A_{s1}^* A_{s2} e^{-2ik_{s1}s} + A_{s2}^* A_{s1} e^{+2ik_{s1}s} \right)}, \quad (7)$$

respectively. It can be observed that the helices of the individual wave are given by the ratios of the corresponding polarization ellipticities to energy densities [12,24,43]. Thus, the concept of the interlink between the EM helices and their local wavevectors is intrinsically based on the decomposition of the energy density and mean wavevector. Noteworthily, the same conclusions can be reached by calculating the two-waves interference in free space ([Supplemental Text V](#)). Thus, from the former analysis, we can conclude that, even in a general framework, the T-spins are originated from the inhomogeneity of EM field while the L-spins are determined by the optical helices solely. Noteworthily, besides the helix-independent T-spins (Figs. 2D and 2E), if the individual wave of two-waves interference system carries EM helix, there must be inhomogeneity of helical density and thus the helix-dependent T-spin will be present (Figs. 2F and 2G). More interesting, we also discover the extraordinary L-spins (Figs. 3H and 3I). Although these L-spins are perpendicular to the mean wavevector (Figs. 3B and 3C), they do not possess the property of spin-momentum locking. Thus, as the propagating directions of these two waves are inverted, the corresponding L-spins remain unchanged, while the directions of helix-independent and helix-dependent T-spins are inverted simultaneously owing to the property of spin-momentum locking.

In addition, the integration of equations (1) and (2) is $\langle \mathbf{S} \rangle = \langle \hbar \sigma_1 \hat{\mathbf{k}}_1 \rangle + \langle \hbar \sigma_1 \hat{\mathbf{k}}_1 \rangle + \langle \mathbf{S}_t \rangle$ (We must mention that the integration of angular momenta would be diverging in the whole three-dimensional space due to the propagating property of EM field. Thus, the integral angular momenta in our manuscript are carried out in a two-dimensional plane, as the techniques introduced in Refs. 2 and 43. And it is unnecessary to calculate the integration in the other half-space if one considers the evanescent wave system since we have proof that the evanescent wave has a similar spin-orbit behavior in that half-space in Ref. 22.), which indicates the integral of the crossed helix vanishes. Thus, the interferential effect is local and does not affect the conservation of AMs ([Supplemental Texts IV and V](#)). Noteworthily, in a rotating symmetric system such as the propagating wave in free space, the total AM is conservative and the integral T-spin is zero. Whereas for an inverse symmetry broken system such as the evanescent wave at an interface, only z -component total AM is conservative, and hence the T-spin can carry net SAM and the integral T-spin is nonvanishing.

From the former analysis, one can realize that there is a phase inhomogeneity caused by the propagating phase. However, this dynamical phase would not give rise to the T-spin, but the T-spin is closely related to the geometric phase. From Eq. 3, it can be found that the helix-dependent T-spin is antiparallel to the local wavevector. Actually, this is a general property of T-spin and widely exist in a generic EM field. For a single polarized EM field, the momentum can be expressed as $\mathbf{\Pi} \propto \langle \Psi | i\nabla | \Psi \rangle$ with $|\Psi\rangle$ representing the potential [13,19,54], the T-spin can be given by $\mathbf{S}_t \propto \nabla \times \mathbf{\Pi} \propto \langle \nabla \Psi | \times i | \nabla \Psi \rangle$, which has a similar form with the Berry curvature of the potential. Moreover, for a generic EM field, the T-spin calculated by $\nabla \times \mathbf{\Pi}$ also has a similar structure as the quantum 2-form [55] that generates the Berry phase associated with a circuit ([Supplemental Text VIII](#)). Previously, the generation of this inverted helical component was explained based on the evolution of geometric phase in EM systems [2]. Here, this inverted helical component can be classified to helix-dependent T-spin which demonstrate the T-spin is closely related to the Berry curvature and the evolution of geometric phase in the EM systems (see [Supplemental Text IX](#) for an example of focused circular polarizations). Moreover, we formulate four Maxwell-like spin-momentum equations and a Helmholtz-like equation in [Table 1](#), which can be utilized to investigate the intrinsic properties of spin AM and momentum for a generic EM wave.

To validate the extraordinary properties of EM spins, we build the scanning imaging systems to mapping the three components of SAMs for the focused circularly polarized lights separately (see [Supplemental Texts X and XI](#)). The experimental results in Fig. 3 reveal that the two transverse components of SAM in the focused field remain unchanged as the incident light alters from right-handed circular polarization (RCP) to left-handed circular polarization (LCP), which is corresponding to the helix-independent T-spin. On the contrary, from the derivations (see [Supplemental Text IX](#)), the z component SAM contains two parts: the L-spin and the extraordinary helix-dependent T-spin. Thus, as the incident optical helices are opposite, the total T-spins will be deflected. Then, together with the reversal of propagating direction, it can be demonstrated that the helix-dependent T-spin of focused circular polarized light processes the $\mathbb{Z}4$ topological invariance, which matches well with theoretical analyses.

Discussions and conclusions: To summarize, we uncover and demonstrate, both theoretically and experimentally, the underlying physical difference between the T-spin and L-spin. First, the L-spin is determined by the EM helix, while the T-spin is originated from the inhomogeneities of EM field. Second, even in a generic EM wave field carrying helices, the T-spin is locked with the momentum of EM field, while the L-spin does not possess the property of spin-momentum locking. We emphasize here that the spin-momentum locking of T-spin is originated from the intrinsic SOI feature of the Maxwell's theory in real space, which is different from the spin-momentum locking by engineering the extrinsic SOI in topological photonics [53]. However, the resulted phenomena of these two physical processes are analogous. There does not exist an EM state whose T-spin vector can be positive and negative concurrently as it propagates in a direction. Akin to topological photonics, one can also design artificial photonic structures sustaining the desired structured light and spin states to achieve the on-chip applications [56]. Third, from the rigorous argument, we discover a helix-dependent T-spin accompanied with a helix-dependent spin-momentum locking. In rotational symmetric system, the integral T-spin vanishes, which is consistent with the principle of conservation of total AM physically. This explains why there is only T-spin exist in the focusing field of an incident wave carrying pure orbital AM. Whereas in a system with broken inverse symmetry, the integral T-spin can be non-zero. Fourth, the T-spin determines the inverted helical component that is arisen from evolution of the Berry curvature of EM systems. Noteworthily, the properties of helix, spin-momentum locking and Berry curvature related T-spins in a generic EM field are different from those of the T-spins of a single polarized mode dramatically. The primary properties of these two spins and their distinction are exhibited in [Table 2](#). Moreover, whether the L-spin or the T-spin, they can be arranged in three-dimensional, and thus the structured property of T-spin can be flexibility designed to obtain various photonic chiral spin textures. The findings deepen our understanding of EM spin and explore the novel applications in manipulation (see [Supplemental Text XII](#)), imaging, communication, nanometrology and on-chip optoelectronic devices.

Acknowledgements

This work was supported, in part, by Guangdong Major Project of Basic Research No. 2020B0301030009, National Natural Science Foundation of China grants 61935013, 62075139, 61427819, 61622504, and 12174266, leadership of Guangdong province program grant 00201505, Science and Technology Innovation Commission of Shenzhen grants JCYJ20200109114018750, Shenzhen Peacock Plan KQTD20170330110444030. L.D. acknowledges the support given by the Guangdong Special Support Program.

Author contributions

P.S. developed the concept. All authors contribute to the manuscript.

Competing interests

The authors declare no competing interests.

Data availability

The data that support the plots within this paper and other findings of this study are available from the corresponding author upon reasonable request.

References:

1. A. Fert, Nobel Lecture: Origin, development, and future of spintronics, *Rev. Mod. Phys.* **80**, 1517 (2004).
2. K. Y. Bliokh, F. J. Rodríguez-Fortuño, F. Nori, and A. V. Zayats, Spin–orbit interactions of light, *Nat. Photon.* **9**(12), 796–808 (2015).
3. W. Yuan, C. Yang, D. Zhang, Y. Long, Y. Pan, Z. Zhong, H. Chen, J. Zhao, and J. Ren, Observation of elastic spin with chiral meta-sources, *Nat. Commun.* **12**, 6954:1-9 (2021).
4. F. Khosravi, M. M. Sonner, and Z. Jacob, Ultrafast electron cycloids driven by the transverse spin of a surface acoustic wave, *Sci. Adv.* **7**, eabf7414:1-7 (2021).
5. S. Wang, G. Zhang, X. Wang, Q. Tong, Jensen Li, and G. Ma, Spin-orbit interactions of transverse sound, *Nat. Commun.* **12**, 6125 (2021).
6. J. B. Gorce, K. Y. Bliokh, H. Xia, N. Francois, H. Punzmann, M. Shats, Rolling spinners on the water surface, *Sci. Adv.* **7**(16), eabd4632 (2021).
7. K. Y. Bliokh, H. Punzmann, H. Xia, F. Nori, M. Shats, Field theory spin and momentum in water waves, *Sci. Adv.* **8**(3), abm1295 (2022).
8. S. Golat, E. A. Lim, and F. J. Rodríguez-Fortuño, Evanescent gravitational waves, *Phys. Rev. D* **101**, 084046 (2020).
9. S. Xin, Y. Long and Jie Ren, Spin angular momentum of gravitational wave interference, *New J. Phys.* **23**, 043035 (2021).
10. A. Aiello, P. Banzer, M. Neugebauer, and G. Leuchs, From transverse angular momentum to photonic wheels, *Nat. Photon.* **9**(12), 789–795 (2015).
11. M. Neugebauer, T. Bauer, A. Aiello, and P. Banzer, Measuring the transverse spin density of light, *Phys. Rev. Lett.* **114**, 063901:1-5 (2015).
12. A.Y. Bekshaev, K. Y. Bliokh, and F. Nori, Transverse spin and momentum in two-wave interference, *Phys. Rev. X* **5**, 011039:1–9 (2015).
13. P. Shi, L. Du, C. Li, A. Zayats, and X. Yuan, Transverse spin dynamics in structured electromagnetic guided waves, *Proc. Natl. Acad. Sci. USA.* **118**(6), e2018816118:1-6 (2021).
14. K. Y. Bliokh, D. Smirnova, and F. Nori, Quantum spin Hall effect of light, *Science* **348**, 1448–1451 (2015).
15. T. Van Mechelen and Z. Jacob, Universal spin-momentum locking of evanescent waves, *Optica* **3**(2), 118-126 (2016).
16. J. S. Eismann, L. H. Nicholls, D. J. Roth, M. A. Alonso, P. Banzer, F. J. Rodríguez-Fortuño, A. V. Zayats, F. Nori, and K. Y. Bliokh, Transverse spinning of unpolarized light, *Nat. Photon.* **15**, 156-161 (2020).
17. L. Du, A. Yang, A. V. Zayats, and X. Yuan, Deep-subwavelength features of photonic skyrmions in a

confined electromagnetic field with orbital angular momentum, *Nat. Phys.* **15**, 650–654 (2019).

18. Y. Dai, Z. Zhou, A. Ghosh, R. S. K. Mong, A. Kubo, C.-B. Huang, and H. Petek, Plasmonic topological quasiparticle on the nanometre and femtosecond scales, *Nature* **588**, 616-619 (2020).
19. X. Lei, A. Yang, P. Shi, Z. Xie, L. Du, Anatoly V. Zayats, and X. Yuan, Photonic spin lattices: symmetry constraints for skyrmion and meron topologies, *Phys. Rev. Lett.* **127**, 237403:1-6 (2021).
20. S. Tsesses, K. Cohen, E. Ostrovsky, B. Gjonaj, and G. Bartal, Spin–orbit interaction of light in plasmonic lattices, *Nano Lett.* **19**(6), 4010–4016 (2019).
21. C. Li, P. Shi, L. Du, and X. Yuan, Mapping the near-field spin angular momenta in the structured surface plasmon polariton field, *Nanoscale* **12**, 13674-13679 (2020).
22. P. Shi, L. Du, and X. Yuan, Strong spin–orbit interaction of photonic skyrmions at the general optical interface, *Nanophotonics* **9**(15): 4619-4628 (2020).
23. A. Ghosh, S. Yang, Y. Dai, Z. Zhou, T. Wang, C. Huang, and H. Petek, A topological lattice of plasmonic merons, *Applied Physics Reviews* **8**, 041413 (2021).
24. P. Shi, L. Du, X. Yuan, Spin photonics: from transverse spin to photonic skyrmions, *Nanophotonics* **10**(16), 3927-3943 (2021).
25. P. Shi, A. Yang, F. Meng, J. Chen, Y. Zhang, Z. Xie, L. Du, and X. Yuan, Optical near-field measurement for spin-orbit interaction of light, *Progress in Quantum Electronics* **78**, 100341:1-20 (2021).
26. M. Antognazzi, C. R. Bermingham, R. L. Harniman, S. Simpson, J. Senior, R. Hayward, H. Hoerber, M. R. Dennis, A. Y. Bekshaev, K. Y. Bliokh and F. Nori, Direct measurements of the extraordinary optical momentum and transverse spin-dependent force using a nano-cantilever, *Nat. Phys.* **12**, 731-735 (2016).
27. P. Shi, L. Du, and X.-C. Yuan, Structured spin angular momentum in highly focused cylindrical vector vortex beams for optical manipulation, *Opt. Express* **26**(8), 23449–23459 (2018).
28. S. Pendharker, F. Kalhor, T. Van Mechelen, S. Jahani, N. Nazemifard, T. Thundat, and Z. Jacob, Spin photonic forces in non-reciprocal waveguides, *Optics Express* **26**(18), 23898-23910 (2018).
29. F. J. Rodríguez-Fortuño, G. Marino, P. Ginzburg, D. O’Connor, A. Martínez, G. A. Wurtz, A. V. Zayats, Near-field interference for the unidirectional excitation of electromagnetic guided modes, *Science* **340**, 328–330 (2013).
30. J. Petersen, J. Volz, and A. Rauschenbeutel, Chiral nanophotonic waveguide interface based on spin–orbit interaction of light, *Science* **346**(6205), 67–71 (2014).
31. Z. Jacob and T. Van Mechelen, Unidirectional Maxwellian spin waves, *Nanophotonics*, **8**(8), 1399-1416 (2019).
32. Z. Guo, Y. Long, H. Jiang, J. Ren, and H. Chen, Anomalous unidirectional excitation of high-k hyperbolic modes using all-electric metasources, *Advanced Photonics* **3**(3), 036001:1-10 (2021).
33. G. Araneda, S. Walser, Y. Colombe, D. B. Higginbottom, J. Volz, R. Blatt, and A. Rauschenbeutel, Wavelength-scale errors in optical localization due to spin–orbit coupling of light, *Nat. Phys.* **15**, 17–21 (2019).
34. J. Zhou, S. Liu, H. Qian, Y. Li, H. Luo, S. Wen, Z. Zhou, G. Guo, B. Shi, Z. Liu, Metasurface enabled quantum edge detection, *Sci. Adv.* **6** (51), eabc4385:1-7 (2020).
35. J Zhou, H Qian, CF Chen, J Zhao, G Li, Q Wu, H Luo, S Wen, Z Liu, Optical edge detection based on high-efficiency dielectric metasurface, *Proc. Natl. Acad. Sci. USA.* **116**(23), 11137-11140 (2019).
36. Z. Shao, J. Zhu, Y. Chen, Y. Zhang, and S. Yu, Spin-orbit interaction of light induced by transverse spin angular momentum engineering, *Nat. Commun.* **9**, 926:1–11 (2018).

37. X. Lei, L. Du, X. Yuan and Anatoly V. Zayats, Optical spin–orbit coupling in the presence of magnetization: photonic skyrmion interaction with magnetic domains, *Nanophotonics* **10**(14), 3667–3675 (2021).

38. L. Du, A. Yang, and X. Yuan, Ultrasensitive displacement sensing method and device based on local spin characteristics, US Patent App. 16/303,773 (2021).

39. P. Lodahl, S. Mahmoodian, S. Stobbe, A. Rauschenbeutel, P. Schneeweiss, J. Volz, H. Pichler, and P. Zoller, Chiral quantum optics, *Nature* **541**, 473–480 (2017).

40. A. Forbes, Michael de Oliveira, and Mark R. Dennis, Structured light, *Nat. Photon.* **15**, 253–262 (2021).

41. H. Rubinsztein-Dunlop, *et. al.*, Roadmap on structured light, *J. Opt.* **19**, 013001 (2017).

42. O. V. Angelsky, A. Y. Bekshaev, S. G. Hanson, C. Yu Zenkova, I. I. Mokhun, and Z. Jun, Structured light: ideas and concepts, *Front. Phys.* **8**, 114:1-26 (2020).

43. K. Y. Bliokh and F. Nori, Transverse and longitudinal angular momenta of light, *Phys. Rep.* **592**, 1–38 (2015).

44. S.-B. Wang and C.-T. Chan, Lateral optical force on chiral particles near a surface, *Nat. Commun.* **5**, 3307 (2014).

45. A. Hayat, J. P. Balthasar Mueller, and F. Capasso, Lateral chirality-sorting optical forces, *Proc. Natl. Acad. Sci. USA* **112** (43), 13190-13194 (2015).

46. M. V. Berry and Pragya Shukla, Geometry of 3D monochromatic light: local wavevectors, phases, curl forces, and superoscillations, *J. Opt.* **21**, 064002:1-13 (2019).

47. M. V. Berry, Optical currents, *J. Opt. Pure Appl. Opt.* **11**(9), 094001:1–12 (2009).

48. F. Alpeggiani, K. Y. Bliokh, F. Nori, and L. Kuipers, Electromagnetic helicity in complex media, *Phys. Rev. Lett.* **120**, 243605:1-6 (2018).

49. P. Shi, L. Du, M. Li, and X.-C. Yuan, Symmetry-protected photonic chiral spin textures by spin–orbit coupling, *Laser & Photonics Reviews* **15**, 202000554:1-9 (2021).

50. J. D. Jackson, *Classical Electrodynamics* (Wiley, ed. 3, 1999).

51. A. V. Zayats, I. I. Smolyaninov, and A. A. Maradudin, Nano-optics of surface plasmon polaritons, *Phys. Rep.* **408**, 131-314 (2005).

52. Y. Kuai, J. Chen, X. Tang, Y. Xiang, F. Lu, C. Kuang, L. Xu, W. Shen, J. Cheng, H. Gui, G. Zou, P. Wang, H. Ming, J. Liu, X. Liu, Joseph R. Lakowicz, and D. Zhang, Label-free surface-sensitive photonic microscopy with high spatial resolution using azimuthal rotation illumination, *Sci. Adv.* **5**, eaav5335:1-10 (2019).

53. T. Ozawa, H. M. Price, A. Amo, N. Goldman, M. Hafezi, L. Lu, M. C. Rechtsman, D. Schuster, J. Simon, O. Zilberberg, and I. Carusotto, Topological photonics, *Rev. Mod. Phys.* **91**, 015006:1-76 (2019).

54. E. Wolf, A scalar representation of electromagnetic fields: II, *Proc. Phys. Soc.* **74**, 269-280 (1959).

55. M. V. Berry, Quantal phase factors accompanying adiabatic changes. *Proc. R. Soc. A* **392**, 45–57 (1984).

56. L. Peng, L. Duan, K. Wang, F. Gao, L. Zhang, G. Wang, Y. Yang, H. Chen, and S. Zhang, Transverse photon spin of bulk electromagnetic waves in bianisotropic media, *Nat. Photon.* **13**, 878–882 (2019).

Figures and Figure captions:

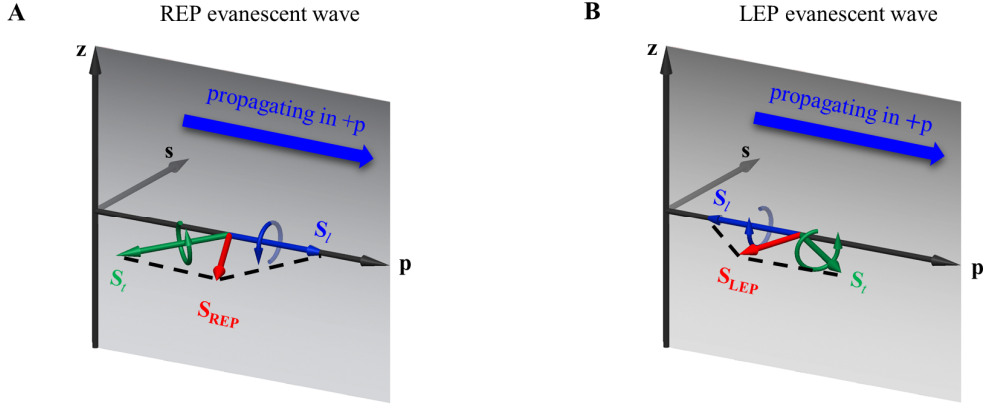


Fig. 1. EM spins of evanescent waves and their spin-momentum locking properties. **A**, the EM spin of a right-handed elliptically polarized (REP) evanescent plane wave; **B**, the EM spin of a left-handed elliptically polarized (LEP) evanescent plane wave. The EM spins contain two parts: L-spin determined by EM helix $\mathbf{S}_l = \hbar\sigma\hat{\mathbf{k}}$ and T-spin \mathbf{S}_t originated from the transverse inhomogeneities of EM fields. Here, there are two types of inhomogeneities: the inhomogeneities of helical density in the sz -plane normal to p -axis and the inhomogeneity of intensity in the zp -plane normal to s -axis. Thus, the T-spins also have two components (s and p components). Noteworthily, the p component T-spin originated from the inhomogeneity of helical density is helix-dependent, while the s -component is helix-independent, which is consistent with the EM spin of the single polarized evanescent plane wave. Here, we only exhibit the spin properties for the waves propagating in $+p$ direction. If the propagating direction is opposite, the helix-dependent components remain unchanged and the helix-independent components are inverted. Thus, there are 4 spin-momentum locking states exist in the EM system, which demonstrates that the photons satisfy the $\mathbb{Z}4$ topological invariance.

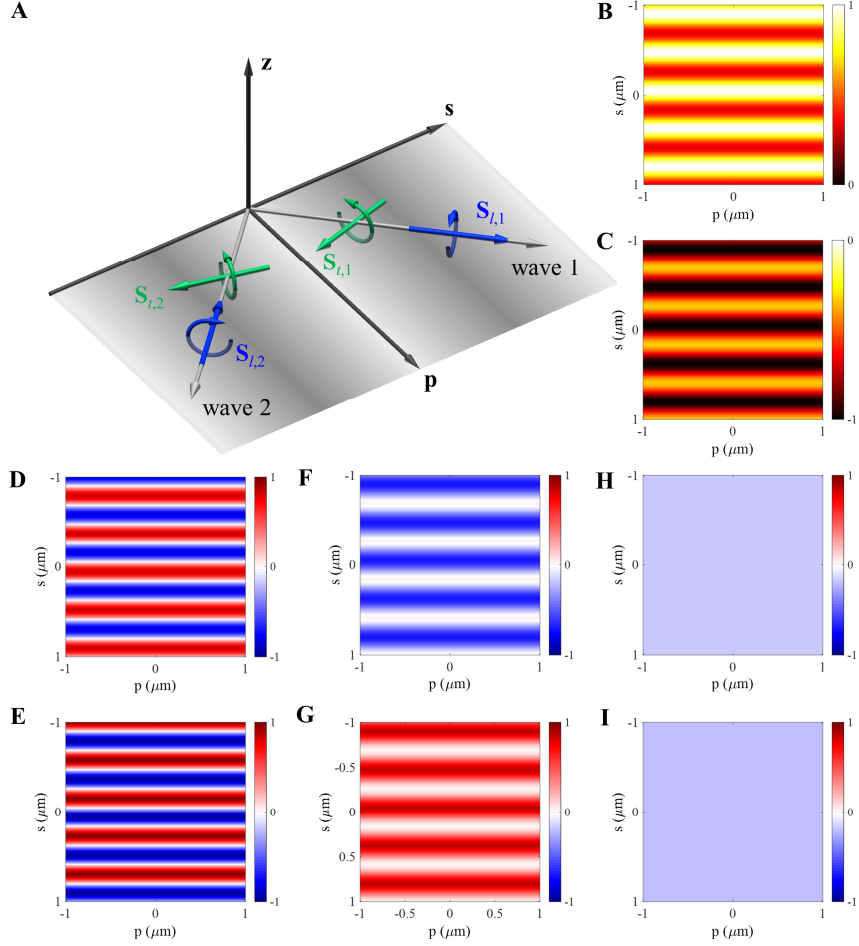


Fig. 2. Spin properties of interferential field between two elliptically polarized evanescent plane waves.

A, Schematic diagram of interferential field in ps -plane between two evanescent plane waves carrying opposite helices. **B**, **C**, the spatial distributions of canonical momenta (only contains p -component) and the corresponding **D**, **E**, z -component helix-independent T-spins, **F**, **G**, s -component helix-dependent T-spins and **H**, **I**, s -component extraordinary L-spins. The canonical momentum determines the mean wavevector and the propagating direction. Here, the whole z -component SAMs are corresponding to the helix-independent T-spins. However, although the s -component SAMs are perpendicular to the mean wavevector, they contain two parts: the helix-dependent T-spins and the extraordinary L-spins. It can be observed that, as the canonical momenta are opposite, the s -component L-spins remain unchanged while the z -component T-spins are inverted. Here, $A_{p1} = A_{p2} = 1$, $A_{s1} = 5 + 2i$ and $A_{s2} = 5 - 2i$; the wavelength is 632.8nm.

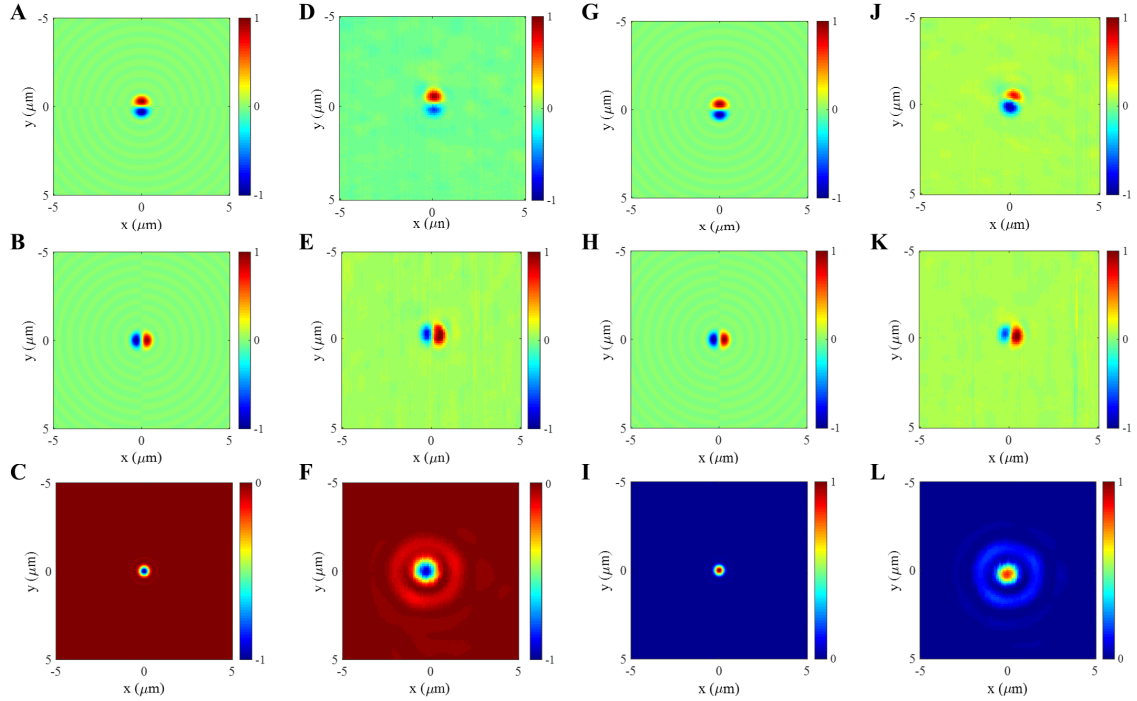


Figure 3. Experimental validation of the spin-momentum locking and T-spin. The theoretical **A**, S_x , **B**, S_y and **C**, S_z and the corresponding experimental **D**, S_x , **E**, S_y and **F**, S_z of the focused LCP light; the theoretical **G**, S_x , **H**, S_y and **I**, S_z and the corresponding experimental **J**, S_x , **K**, S_y and **L**, S_z of the focused RCP light. Here, we use the traditional Cartesian coordinates (x, y, z) instead of orthogonal coordinates (p, s, z). The optical axis is along the z -direction. The experimental SAM distributions match well with those of theoretical results. The details of theoretical calculations can be found in [Supplemental Text IX](#). The experimental results and the corresponding error analysis can be found in [Supplemental Texts X and XI](#). As the incident wave is changed from the LCP light to RCP light, the x and y components of SAMs, which can be regarded as the helix-independent T-spin, remain unchanged. On the contrary, the sign of z component of SAM alters from positive to negative as the helix of incident light changes. The z component of SAM contains two parts: the L-spin and the helix-dependent T-spin. Thus, the total T-spin is deflected slightly with respect to the pure helix-independent T-spin. Together with the inverted propagating direction, it can be demonstrated that the helix-dependent T-spin of focused circular polarized light processes the $\mathbb{Z}4$ topological invariance, which matches well with theoretical analyses. The wavelength is fixed at 632.8nm in the experiments. The scanned region is $10\mu\text{m} \times 10\mu\text{m}$ and the grid size is 100nm. The (**D**, **E**, **J**, **K**) is normalized to the maximum and the numerical aperture of this focusing system is 0.5; and the (**F**, **L**) is normalized to their maximum and the numerical aperture of this focusing system measured the S_z is 0.7.

Table 1. Maxwell-like spin-momentum equations and Helmholtz-like equation of a generic EM field

Maxwell-like Spin-momentum equations
$\nabla \cdot \mathbf{\Pi} = 0$
$\nabla \cdot \mathbf{S} = 0$
$\nabla \times \mathbf{\Pi} = 2k^2 (\mathbf{S} - \mathbf{S}_l)$
$\nabla \times \mathbf{S} = 2(\mathbf{\Pi} - \mathbf{P})$
Helmholtz-like equation
$\nabla^2 \mathbf{S} + 4k^2 (\mathbf{S} - \mathbf{S}_l) = 2\nabla \times \mathbf{P}$

Table 2. Underlying physical properties of T-spin and L-spins for a generic EM field

Properties	EM T-spin	EM L-spin
Physical origin	Transverse inhomogeneities	EM helix σ
Does it carry energy?	Does not carry	Carry
Deterministic equation	$\mathbf{S}_t = \frac{1}{2k^2} \nabla \times \mathbf{H}$	$\mathbf{S}_l = \hbar \sigma \otimes \hat{\mathbf{k}}$
Direction of spin vector	Antiparallel and perpendicular to local wave vector $\hat{\mathbf{k}}$.	Parallel to local wave vector $\hat{\mathbf{k}}$.
Is locked with momentum?	Yes.	No.
Is local helix-dependent?	Yes if there is inhomogeneity of helical density.	Yes.
Is integral helix-dependent?	Yes in the system with broken rotating symmetry.	Yes.
Is related to Berry curvature?	Yes.	Yes.

Supplementary Materials for

“Spin decomposition and topological properties in a generic electromagnetic field”

Peng Shi*, Aiping Yang, Xiaojin Yin, Xinrui Lei, Luping Du*, Xiaocong Yuan*

Nanophotonics Research Centre, Shenzhen Key Laboratory of Micro-Scale Optical Information Technology, Institute of micro/nano optoelectronics, Shenzhen University, Shenzhen, 518060, China

*Authors to whom correspondence should be addressed: pittshiustc@gmail.com, lpdu@szu.edu.cn and xcyuan@szu.edu.cn.

Contents:

- I. Basic dynamical physical quantities in spin-orbit interaction of light
- II. Spin properties of elliptically polarized propagating plane waves
- III. Spin properties of elliptically polarized evanescent plane waves
- IV. Spin properties of interferential evanescent plane waves
- V. Spin properties of interferential propagating plane waves
- VI. Spin-momentum equations for the generic electromagnetic field
- VII. Nontrivial spin Chern number of arbitrary structured electromagnetic waves
- VIII. Transverse spin and Berry curvature
- IX. Spin properties of focusing circular polarization light in free space
- X. Experimental setup and measurement of SAM parallel to the optical axis
- XI. Experimental setup and measurement of SAM parallel to optical axis
- XII. Transverse optical forces by spin-momentum locked photonic skyrmions

I. Basic dynamical physical quantities in spin-orbit interaction of light

To investigate the spin-orbit interaction of a time-harmonic monochromatic electromagnetic (EM) field (\mathbf{E} : electric field; \mathbf{H} : magnetic field) with angular frequency ω in a lossless isotropic medium with permittivity ϵ and permeability μ , we first introduce the expressions of the cycle-averaged energy density W , kinetic momentum density $\mathbf{\Pi}$, canonical momentum density \mathbf{P} and total spin angular momentum (SAM) density \mathbf{S} as follows (SI units are used through the manuscript and supplemental materials):

$$W = \langle \psi | \psi \rangle = \frac{1}{4} \{ \epsilon \mathbf{E}^* \cdot \mathbf{E} + \mu \mathbf{H}^* \cdot \mathbf{H} \}, \quad (\text{S.1})$$

$$\mathbf{P} = \frac{1}{\hbar \omega} \langle \psi | \hat{\mathbf{P}} | \psi \rangle = \frac{1}{4\omega} \text{Im} \{ \epsilon \mathbf{E}^* \cdot (\nabla) \mathbf{E} + \mu \mathbf{H}^* \cdot (\nabla) \mathbf{H} \}, \quad (\text{S.2})$$

$$\mathbf{\Pi} = \langle \psi | \hat{\mathbf{r}}/v | \psi \rangle = \frac{1}{2v^2} \text{Re} \{ \mathbf{E}^* \times \mathbf{H} \}, \quad (\text{S.3})$$

and

$$\mathbf{S} = \frac{1}{\hbar \omega} \langle \psi | \hat{\mathbf{S}} | \psi \rangle = \frac{1}{4\omega} \text{Im} \{ \epsilon (\mathbf{E}^* \times \mathbf{E}) + \mu (\mathbf{H}^* \times \mathbf{H}) \}. \quad (\text{S.4})$$

Here, the vector $|\psi\rangle = [\sqrt{\epsilon}\mathbf{E}, i\sqrt{\mu}\mathbf{H}]^T/2$ represents the photon wave function [S1-S7] and the symbol T represents the transpose of matrix; $\mathbf{X} \cdot (\nabla) \mathbf{Y} \equiv \sum_i x_i \nabla y_i$; $\hat{\mathbf{P}} = -i\hbar \nabla$ denotes the momentum operator in quantum mechanics; the symbol $\hat{\mathbf{r}}/v = [\mathbf{0}, \hat{\mathbf{S}}/v; \hat{\mathbf{S}}/v, \mathbf{0}]$ denotes the kinetic momentum operator with $v = 1/\sqrt{\epsilon\mu}$ being the velocity of light in medium and $\hat{\mathbf{S}}$ is the spin-1 matrix in SO(3) [13]; \hbar is the reduced Plank constant and the symbol $*$ indicates the complex conjugate. Here, we do not consider the dispersion [48], which will induce an additional group term in the permittivity and permeability.

It is worth noting that, from the spin-orbit decomposition proposed by M. V. Berry [S1], the kinetic momentum $\mathbf{\Pi}$ can be decomposed into the orbital momentum (which is also considered as the canonical momentum) and Belinfante spin momentum ($\mathbf{P}_s = \nabla \times \mathbf{S}/2$): $\mathbf{\Pi} = \mathbf{P} + \mathbf{P}_s$. Therein, the orbital/canonical momentum \mathbf{P} can naturally be associated with the local wavevector of the field as $\bar{\mathbf{k}} = \mathbf{P}/\hbar$ with its directional vector $\hat{\mathbf{k}} = \bar{\mathbf{k}}/k$ and modulus $k = |\bar{\mathbf{k}}| = \omega \sqrt{\epsilon\mu}$ [S2].

Naturally, in the passive homogeneous space, there are:

$$\nabla \cdot \mathbf{\Pi} = 0, \quad (\text{S.5})$$

$$\nabla \cdot \mathbf{S} = 0, \quad (\text{S.6})$$

$$\mathbf{\Pi} = \mathbf{P} + \mathbf{P}_s, \quad (\text{S.7})$$

and

$$\mathbf{P}_s = \nabla \times \mathbf{S}/2 . \quad (\text{S.8})$$

The former equations (S.5-S.8) have been proposed in plentiful references [2, 13, 24, 25, 43]. Here, we aim to investigate the spin decomposition into the longitudinal spin (L-spin) and the transverse spin (T-spin) for a generic EM field (akin to the Helmholtz decomposition of an arbitrary vector mathematically) in free space or at the interface, and the resulted spin-momentum topological properties.

II. Spin properties of elliptically polarized propagating plane waves

Elliptically polarized propagating plane wave

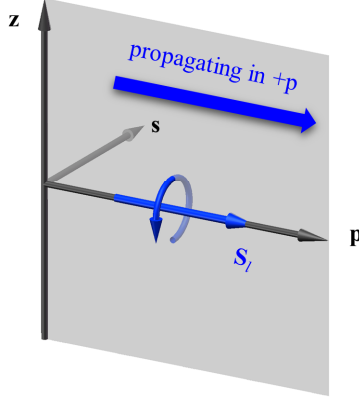


Fig. S1. The schematic diagram of elliptically polarized plane wave propagating in $+p$ -direction. Only the L-spin exists in the case.

In this section, we will investigate the dynamical properties of propagating EM plane waves. The dynamical properties of the propagating EM plane waves have been studied by many researchers [24, 25, 43] and thus we directly summarize the main results here. Assuming the electric field components of a plane wave propagating in the p -direction (in Fig. S1) at an arbitrary orthogonal coordinate system (p, s, z) as: $\mathbf{E} = (0\hat{\mathbf{p}} + A_s\hat{\mathbf{s}} + A_p\hat{\mathbf{z}})e^{i(kp-\omega t)}$, the magnetic field components are: $\mathbf{H} = (0\hat{\mathbf{p}} - A_p\hat{\mathbf{s}} + A_s\hat{\mathbf{z}})e^{i(kp-\omega t)} / \eta$, where $\eta = \sqrt{\mu/\epsilon}$ is the wave impedance, A_s, A_p are the complex amplitudes of s -polarization and p -polarization components, respectively. Since the EM wave considered here is time-harmonic throughout, we ignore the $\exp(-i\omega t)$ in the following expressions. From the expressions of electric field and magnetic field, it can be deduced that the energy density and the canonical momentum are

$$W = \frac{1}{4} \{ \epsilon |\mathbf{E}|^2 + \mu |\mathbf{H}|^2 \} = \frac{\epsilon}{2} \{ A_s^* A_s + A_p^* A_p \}, \quad (\text{S.9})$$

$$\mathbf{P} = \frac{1}{4\omega} \text{Im} \{ \epsilon \mathbf{E}^* \cdot (\nabla) \mathbf{E} + \mu \mathbf{H} \cdot (\nabla) \mathbf{H} \} = \frac{W}{\omega} (k\hat{\mathbf{p}} + 0\hat{\mathbf{s}} + 0\hat{\mathbf{z}}), \quad (\text{S.10})$$

respectively. The local wavevector is determined by the canonical momentum as

$$\bar{\mathbf{k}} = \frac{\mathbf{P}}{\hbar\omega} = \frac{W}{\hbar\omega} (k\hat{\mathbf{p}} + 0\hat{\mathbf{s}} + 0\hat{\mathbf{z}}), \quad (\text{S.11})$$

with its unit directional vector

$$\hat{\mathbf{k}} = \frac{\bar{\mathbf{k}}}{k} = \frac{W}{\hbar\omega} (1\hat{\mathbf{p}} + 0\hat{\mathbf{s}} + 0\hat{\mathbf{z}}). \quad (\text{S.12})$$

In this way, the canonical momentum can be rewritten as $\mathbf{P} = \hbar\bar{\mathbf{k}} = \hbar k \hat{\mathbf{k}}$, which is consistent with that

of in quantum physics [S1]. Then, the SAM is

$$\mathbf{S} = \frac{W}{\omega} \left(\frac{\text{Im} \{ A_s^* A_p - A_p^* A_s \}}{A_s^* A_s + A_p^* A_p} \hat{\mathbf{p}} + 0\hat{\mathbf{s}} + 0\hat{\mathbf{z}} \right) = \hbar \sigma \frac{\bar{\mathbf{k}}}{k} = \hbar \sigma \hat{\mathbf{k}}. \quad (\text{S.13})$$

Equation (S.13) shows that the spin vector is parallel to the local wavevector, and thus the researchers named this type of spin as L-spin \mathbf{S}_l . Noteworthily, the EM helix σ is defined as [43]

$$\sigma = \frac{\text{Im} \{ A_s^* A_p - A_p^* A_s \}}{A_s^* A_s + A_p^* A_p}. \quad (\text{S.14})$$

Here, the numerator represents the polarization ellipticity of EM field and the denominator is proportional to energy density (S.9). It is obvious that the time-averaging physical quantities of this propagating plane wave is homogeneous in space, including the intensity and polarization homogeneities (Actually, there is phase inhomogeneity due to the dynamical phase variation. However, the dynamical phase variations would not cause the T-spin and whereas in the section VIII, we will show that the T-spin is linked to geometric phase closely.). Thus, it does not have T-spin from [Equation \(1\) in main text](#). The kinetic momentum is

$$\mathbf{\Pi} = \frac{\epsilon \mu}{2} \text{Re} \{ \mathbf{E}^* \times \mathbf{H} \} = \frac{W}{c} (1\hat{\mathbf{p}} + 0\hat{\mathbf{s}} + 0\hat{\mathbf{z}}) \quad (\text{S.15})$$

and the T-spin given by the vorticity of kinetic momentum is

$$\mathbf{S}_t = \frac{1}{2k^2} \nabla \times \mathbf{\Pi}(\mathbf{r}) = 0. \quad (\text{S.16})$$

In summary, the spin-momentum properties of elliptically polarized plane waves can be summed as:

$$\mathbf{S}_l = \hbar \sigma \hat{\mathbf{k}}, \quad \mathbf{S}_t = \frac{1}{2k^2} \nabla \times \mathbf{\Pi}(\mathbf{r}) = 0 \quad \text{and} \quad \mathbf{S} = \mathbf{S}_l + \mathbf{S}_t, \quad (\text{S.17})$$

which coincides well with the former results in several review papers [2, 10, 24, 25, 43].

III. Spin properties of elliptically polarized evanescent plane waves

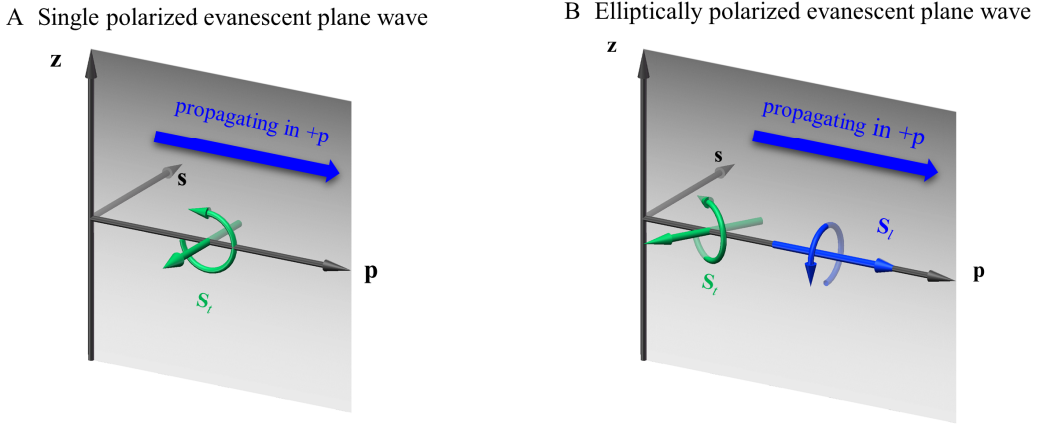


Fig. S2. (A) The schematic diagram of single polarized evanescent plane wave propagating in p -direction at an interface $z = 0$. Only the helix-independent T-spin exists in the case. (B) The schematic diagram of elliptically polarized evanescent plane wave propagating in p -direction at an interface $z = 0$. The L-spin and T-spin exist simultaneously in the case.

In the section, we investigate the spin-momentum properties of evanescent plane waves. We assume the interface is at $z = 0$ and we only consider the evanescent modes at $z > 0$ since the evanescent modes at $z < 0$ has the similar spin-momentum properties [22]. The electric field components of an elliptically polarized evanescent plane wave (decaying exponentially in the $+z$ -direction) can be given by:

$$\mathbf{E} = \left(-A_p \frac{i\kappa}{k} \hat{\mathbf{p}} + A_s \hat{\mathbf{s}} + A_p \frac{k_p}{k} \hat{\mathbf{z}} \right) \exp(ik_p p - \kappa z) \quad (\text{S.18})$$

as shown in [Fig. S2\(B\)](#). Obviously, the electric field satisfies the Gaussian law:

$$\nabla \cdot \mathbf{E} = \left(-A_p \frac{i\kappa}{k} ik_p - A_p \frac{k_p}{k} \kappa \right) \exp(ik_p p - \kappa z) = 0. \quad (\text{S.19})$$

Here, A_s , A_p are the complex amplitudes of s -polarization and p -polarization components, respectively; k , k_p and $i\kappa$ are the total, in-plane and out-of-plane wave vectors, respectively; the wave vectors satisfy the relation: $k_p^2 = k^2 + \kappa^2$. From the expression of electric field, one can obtain the magnetic field as:

$$\mathbf{H} = \frac{1}{\eta} \left(-A_s \frac{i\kappa}{k} \hat{\mathbf{p}} - A_p \hat{\mathbf{s}} + A_s \frac{k_p}{k} \hat{\mathbf{z}} \right) \exp(ik_p p - \kappa z). \quad (\text{S.20})$$

From the electric and magnetic field components, the energy density and the canonical momentum are:

$$W = \frac{\varepsilon}{2} \frac{k_p^2}{k^2} \left\{ A_s^* A_s + A_p^* A_p \right\} e^{-2\kappa z}, \quad (\text{S.21})$$

$$\mathbf{P} = \frac{\varepsilon}{2\omega} \frac{k^3}{k^2} \left(\left\{ A_s^* A_s + A_p^* A_p \right\} \hat{\mathbf{p}} + 0\hat{\mathbf{s}} + 0\hat{\mathbf{z}} \right) e^{-2\kappa z} = \frac{W}{\omega} \left(k_p \hat{\mathbf{p}} + 0\hat{\mathbf{s}} + 0\hat{\mathbf{z}} \right), \quad (\text{S.22})$$

respectively. Both the energy density and the canonical momentum decay exponentially in the $+z$ -direction. Then, the local wave vector of the evanescent plane wave is

$$\bar{\mathbf{k}} = \frac{\mathbf{P}}{\hbar} = \frac{W}{\hbar\omega} \left(k_p \hat{\mathbf{p}} + 0\hat{\mathbf{s}} + 0\hat{\mathbf{z}} \right), \quad (\text{S.23})$$

with its unit directional vector

$$\hat{\mathbf{k}} = \frac{\bar{\mathbf{k}}}{k} = \frac{W}{\hbar\omega} \frac{k_p}{k} \left(1\hat{\mathbf{p}} + 0\hat{\mathbf{s}} + 0\hat{\mathbf{z}} \right). \quad (\text{S.24})$$

Similarly, the canonical momentum of the evanescent plane wave can be rewritten as $\mathbf{P} = \hbar\bar{\mathbf{k}} = \hbar k \hat{\mathbf{k}}$, which is consistent with that in quantum physics.

Subsequently, the SAM can be calculated to be

$$\mathbf{S} = \frac{W}{\omega} \frac{\kappa}{k_p} \left(\frac{k}{\kappa} \frac{\text{Im} \{ A_s^* A_p - A_s A_p^* \}}{A_s^* A_s + A_p^* A_p} \hat{\mathbf{p}} - 1\hat{\mathbf{s}} + 0\hat{\mathbf{z}} \right) = \frac{W}{\omega} \left(+ \frac{k}{k_p} \sigma \hat{\mathbf{p}} - \frac{\kappa}{k_p} \hat{\mathbf{s}} + 0\hat{\mathbf{z}} \right) = \frac{k^2}{k_p^2} \hbar \sigma \hat{\mathbf{k}} - \frac{W}{\omega} \frac{\kappa}{k_p} \hat{\mathbf{s}} + 0\hat{\mathbf{z}}. \quad (\text{S.25})$$

with an EM helix

$$\sigma = \frac{\text{Im} \{ A_s^* A_p - A_s A_p^* \}}{A_s^* A_s + A_p^* A_p}.$$

Here, the numerator of helix represents the polarization ellipticity of EM field and the denominator of helix is proportional to energy density (S.21) of the evanescent waves. Previously, most researches [43] regarded the s -component SAM, which is helix-independent, as the T-spin. This is correct and logical for a single polarized mode ($A_p=0$ or $A_s=0$), as shown in Fig. S2(A). However, it is incomplete for the elliptically polarized evanescent plane wave with EM helix as shown in Fig. S2(B).

In the following, we will analyze the spin properties of the elliptically polarized evanescent plane wave from the point of transverse inhomogeneity given by Eq. 1 and Eq. 2 of main text. First, in the ps -plane, it is obvious that the intensity and polarization are homogeneous (Dynamical phase variation would not produce T-spin). Thus, there is no T-spin exist in the normal direction of ps -plane (z -direction). Second, in the pz -plane, the polarization is homogeneous while the amplitude decays exponentially in the evanescent region. These two conditions result in the inhomogeneity in the density of polarization (defined by the product of polarization degree and energy density). Thus, in the normal direction of pz -plane, one can expect that there is a T-spin exist. Third, in the sz -plane, the EM helix is homogeneous while the intensity is inhomogeneous in the evanescent region. These two conditions lead to the

inhomogeneity in the helical density (defined by the product of helix and energy density). Thus, in the normal direction of sz -plane, it can be expected that there is a helix-dependent T-spin exist. Keep this idea in mind, we calculate the kinetic momentum and the T-spin given by the vorticity of the kinetic momentum as:

$$\mathbf{\Pi} = \left(\frac{k}{k_p} c \right) \frac{W}{c^2} \left(\mathbf{l}\hat{\mathbf{p}} - \frac{\kappa}{k} \frac{\text{Im}\{A_s^* A_p - A_p^* A_s\}}{A_s^* A_s + A_p^* A_p} \hat{\mathbf{s}} + 0\hat{\mathbf{z}} \right) = \left(\frac{k}{k_p} c \right) \frac{W}{c^2} \left(+\mathbf{l}\hat{\mathbf{p}} - \frac{\kappa}{k} \sigma \hat{\mathbf{s}} + 0\hat{\mathbf{z}} \right), \quad (\text{S.26})$$

and

$$\mathbf{S}_t = \frac{1}{2k^2} \nabla \times \mathbf{\Pi} = \frac{W}{\omega} \frac{\kappa}{k_p} \left(-\frac{\kappa}{k} \frac{\text{Im}\{A_s^* A_p - A_p^* A_s\}}{|A_s|^2 + |A_p|^2} \hat{\mathbf{p}} - \mathbf{l}\hat{\mathbf{s}} + 0\hat{\mathbf{z}} \right) = \frac{W}{\omega} \frac{\kappa}{k_p} \left(-\frac{\kappa}{k} \sigma \hat{\mathbf{p}} - \mathbf{l}\hat{\mathbf{s}} + 0\hat{\mathbf{z}} \right). \quad (\text{S.27})$$

Equation (S.27) definitely shows that the T-spin has two components: the s -component is helix-independent and the p -component is helix-dependent. These results are consistent with our analysis from the point of the transverse inhomogeneity.

In the end of this section, we prove that the vorticity of kinetic momentum gives the T-spin in theory by subtracting the vorticity of kinetic momentum (S.27) from the total SAM \mathbf{S} (S.25):

$$\mathbf{S}_l = \mathbf{S} - \frac{1}{2k^2} \nabla \times \mathbf{\Pi} = \frac{W}{\omega} \frac{k_p}{k} \left(\frac{\text{Im}\{A_s^* A_p - A_p^* A_s\}}{|A_p|^2 + |A_s|^2} \hat{\mathbf{p}} + 0\hat{\mathbf{s}} + 0\hat{\mathbf{z}} \right) = \frac{W}{\omega} \frac{k_p}{k} \sigma (\mathbf{l}\hat{\mathbf{p}} + 0\hat{\mathbf{s}} + 0\hat{\mathbf{z}}) = \hbar \sigma \hat{\mathbf{k}}. \quad (\text{S.28})$$

The last term of Eq. (S.28) matches well with that of Eq. (S.17), which indicates the remaining SAM is definitely the L-spin. It is worth noting that there is conservation of z -component total angular momentum instead of SAM owing to the rotational symmetry of the interface system. However, since all the canonical momentum, the local wavevector and the SAM are normalized by the energy density, the former spin-momentum properties can also be referred to a single wave packet. By properly choosing the coordinates to eliminate the extrinsic orbital angular momentum, one can conclude that there will be conservation of intrinsic SAM of a single wave packet when the intrinsic orbital angular momentum (vortex phase) is absence, although the total SAM is never conservative in the nonparaxial system due to the spin-orbit coupling [2].

In summary, the results of elliptically polarized evanescent plane waves can be summed as:

$$\mathbf{S}_l = \hbar \sigma \hat{\mathbf{k}}, \quad \mathbf{S}_t = \frac{1}{2k^2} \nabla \times \mathbf{\Pi} = \frac{W}{\omega} \frac{\kappa}{k_p} \left(-\frac{\kappa}{k} \sigma \hat{\mathbf{p}} - \mathbf{l}\hat{\mathbf{s}} + 0\hat{\mathbf{z}} \right) \quad \text{and} \quad \mathbf{S} = \mathbf{S}_l + \mathbf{S}_t. \quad (\text{S.29})$$

In addition, equation (S.29) represents the spin-momentum locking property in classical EM system. The effect of intrinsic spin-momentum locking originated from the intrinsic spin-orbit coupling of

Maxwell's equations has been investigated intensively by many research groups [13-15, 39]. However, all the former works put emphasis on the spin-momentum locking in single polarized modes. Here, from equation (S.29), it can be found that the spin-momentum locking is also helix-dependent, and a slight deflection is introduced into the vector direction of T-spin as shown in Fig. S3. Thus, there are two pairs of spin-momentum locking states, which are consistent with the nontrivial photonic spin Chern number and satisfy the \mathbb{Z}_4 topological invariance [proof in [Supplemental Text VII](#)].

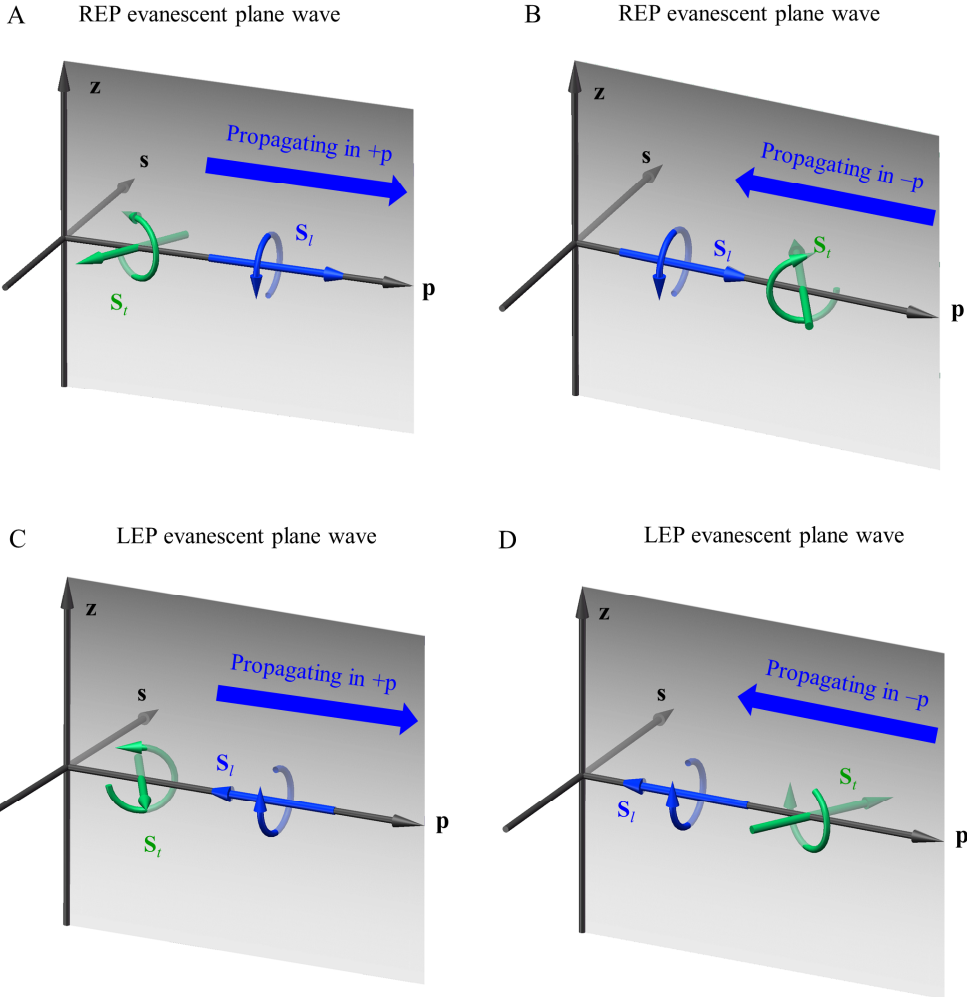


Fig. S3. Spin-momentum locking states of the helix-dependent T-spins. The L-spin and T-spin of right-handed elliptically polarized (REP) evanescent plane wave propagating in the (A) $+p$ -direction and (B) $-p$ -direction; the L-spin and T-spin of left-handed elliptically polarized (LEP) evanescent plane wave propagating in the (C) $+p$ -direction and (D) $-p$ -direction. The p component T-spin originated from the inhomogeneity of helical density is helix-dependent and inverted to the direction of L-spin. Therefore, the direction vector of T-spin for the elliptically polarized evanescent plane wave is deflected compared to that of the single polarized evanescent plane wave in Fig. S2(A).

In the special case that the dual symmetry between the electric and magnetic properties is broken, there is only one polarized state survive at the optical interface (such as: surface plasmons polaritons [51] or Bloch surface wave [52] as shown in [Fig. S2\(A\)](#)). The results can be downgraded into:

$$\mathbf{S}_l = 0, \quad \mathbf{S}_t = \frac{1}{2k^2} \nabla \times \mathbf{\Pi} = \frac{W}{\omega} \frac{\kappa}{k_p} (0\hat{\mathbf{p}} - 1\hat{\mathbf{s}} + 0\hat{\mathbf{z}}) \quad \text{and} \quad \mathbf{S} = \mathbf{S}_l + \mathbf{S}_t, \quad (\text{S.30})$$

which indicate the intrinsic spin-momentum locking of single polarized modes [13-15].

IV. Spin properties of interferential evanescent plane waves

From the superposition theory of states [50], an arbitrary structured light can be expanded into the superposition of plane wave basises. Thus, to draw a clear physical image, we investigate the spin properties of the generic EM field by the superposition of plane waves basis. Here, for the sake of simplicity, we only consider the two-waves interference, but the results can be extended to the situation of the multi-waves interference. The two elliptically polarized evanescent plane waves (waves 1: A_{s1}, A_{p1} ; wave 2: A_{s2}, A_{p2}) propagate in the ps -plane with an intersected angle $2\Theta_1$ between their wave vectors $\mathbf{k}_{1,2} = k_{p1}\hat{\mathbf{p}} \pm k_{s1}\hat{\mathbf{s}} - \kappa\hat{\mathbf{z}}$ where $k_p^2 = k^2 + \kappa^2$, $k_{p1} = k_p \cos\Theta_1$ and $k_{s1} = k_p \sin\Theta_1$ as shown in [Fig. S4](#). The interface is at $z = 0$, and only the evanescent modes in the region $z > 0$ is considered here.

Interference of two elliptically polarized plane waves

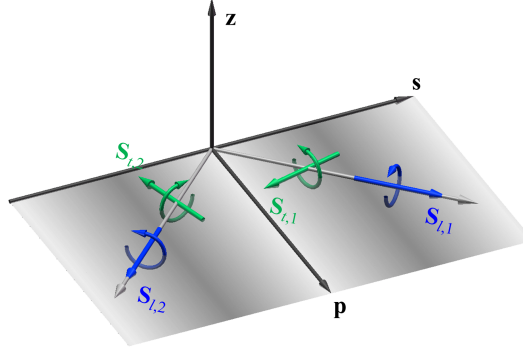


Fig. S4. The schematic diagram of the interference between two elliptically polarized evanescent plane waves. The intersected angle between the individual wave and the p -axis is Θ_1 .

For the individual evanescent plane wave, the energy density, directional vector of local wave vector, and L-spin can be expressed as:

$$W_1 = \frac{\epsilon}{2} \frac{k_p^2}{k^2} \{A_{p1}^* A_{p1} + A_{s1}^* A_{s1}\} e^{-2\kappa z}, \quad W_2 = \frac{\epsilon}{2} \frac{k_p^2}{k^2} \{A_{p2}^* A_{p2} + A_{s2}^* A_{s2}\} e^{-2\kappa z}, \quad (\text{S.31})$$

$$\hat{\mathbf{k}}_1 = \frac{W_1}{\hbar\omega} \frac{k_p}{k} \left(k_{p1}/k_p \hat{\mathbf{p}} + k_{s1}/k_p \hat{\mathbf{s}} + 0\hat{\mathbf{z}} \right), \quad \hat{\mathbf{k}}_2 = \frac{W_2}{\hbar\omega} \frac{k_p}{k} \left(k_{p2}/k_p \hat{\mathbf{p}} - k_{s2}/k_p \hat{\mathbf{s}} + 0\hat{\mathbf{z}} \right), \quad (\text{S.32})$$

and

$$\mathbf{S}_{l,1} = \hbar \frac{\text{Im}\{A_{s1}^* A_{p1} - A_{p1}^* A_{s1}\}}{A_{p1}^* A_{p1} + A_{s1}^* A_{s1}} \hat{\mathbf{k}}_1 = \hbar \sigma_1 \hat{\mathbf{k}}_1, \quad \mathbf{S}_{l,2} = \hbar \frac{\text{Im}\{A_{s2}^* A_{p2} - A_{p2}^* A_{s2}\}}{A_{p2}^* A_{p2} + A_{s2}^* A_{s2}} \hat{\mathbf{k}}_2 = \hbar \sigma_2 \hat{\mathbf{k}}_2. \quad (\text{S.33})$$

These results match well with those of Equations (S.21), (S.24) and (S.28).

Subsequently, for the interference field, the energy density is

$$W = \frac{\epsilon}{2} \frac{k_p^2}{k^2} \left\{ \underbrace{\left[+A_{s1}^* A_{s1} + A_{p1}^* A_{p1} + A_{s2}^* A_{s2} + A_{p2}^* A_{p2} \right]}_{W_1} + \underbrace{\left[+A_{s1}^* A_{s2} e^{-2ik_{s1}s} + A_{s1} A_{s2}^* e^{2ik_{s1}s} + A_{p1}^* A_{p2} e^{-2ik_{s1}s} + A_{p1} A_{p2}^* e^{2ik_{s1}s} \right]}_{W_2} + \underbrace{\left[\frac{k_{p1}^2}{k_p^2} \left(A_{s1}^* A_{s2} e^{-2ik_{s1}s} + A_{s1} A_{s2}^* e^{2ik_{s1}s} + A_{p1}^* A_{p2} e^{-2ik_{s1}s} + A_{p1} A_{p2}^* e^{2ik_{s1}s} \right) \right]}_{W_c} \right\} e^{-2\kappa z} = W_1 + W_2 + W_c \cdot (S.34)$$

Here, the term W_c is originated from the coupling between the two evanescent plane waves and is considered as the coupling energy density.

The total SAM and the T-spin given by the vorticity of kinetic momentum are

$$\mathbf{S} = \frac{\epsilon}{4\omega} \text{Im} \left\{ \begin{array}{l} \left\{ \begin{array}{l} +\frac{i\kappa}{k} \frac{k_{s1}}{k} \left[A_{s1}^* A_{s1} + A_{p1}^* A_{p1} - A_{s2}^* A_{s2} - A_{p2}^* A_{p2} \right] \\ +\frac{k_{p1}}{k} \left[+A_{s1}^* A_{p1} - A_{s1} A_{p1}^* + A_{s2}^* A_{p2} - A_{s2} A_{p2}^* \right. \\ \left. +A_{s1}^* A_{p2} e^{-2ik_{s1}s} - A_{s1} A_{p2}^* e^{2ik_{s1}s} + A_{s2}^* A_{p1} e^{2ik_{s1}s} - A_{s2} A_{p1}^* e^{-2ik_{s1}s} \right] \end{array} \right\} \hat{\mathbf{p}} \\ \left\{ \begin{array}{l} -\frac{i\kappa}{k} \frac{k_{p1}}{k} \left[+A_{s1}^* A_{s1} + A_{p1}^* A_{p1} + A_{s2}^* A_{s2} + A_{p2}^* A_{p2} \right] \\ +\frac{k_{s1}}{k} \left[A_{s1}^* A_{p1} - A_{s1} A_{p1}^* \right. \\ \left. -A_{s2}^* A_{p2} + A_{s2} A_{p2}^* \right] \end{array} \right\} \hat{\mathbf{s}} e^{-2\kappa z}, \\ \left\{ \begin{array}{l} +\frac{k_{p1}}{k} \frac{k_{s1}}{k} \left[+A_{s2}^* A_{s1} e^{+2ik_{s1}s} - A_{s1}^* A_{s2} e^{-2ik_{s1}s} \right. \\ \left. +A_{p2}^* A_{p1} e^{+2ik_{s1}s} + A_{p1}^* A_{p2} e^{-2ik_{s1}s} \right] \end{array} \right\} \hat{\mathbf{z}} \end{array} \right\}$$

and

$$\mathbf{S}_t = \frac{1}{2k^2} \nabla \times \mathbf{\Pi} = \frac{\epsilon}{2\omega} \left\{ \begin{array}{l} \left\{ \begin{array}{l} -\frac{\kappa^2}{k} \frac{k_{p1}}{k} \text{Im} \left[+A_{s1}^* A_{p1} - A_{s1} A_{p1}^* \right] + \frac{\kappa k_{s1}}{k^2} \left[+A_{s1}^* A_{s1} + A_{p1}^* A_{p1} \right] \\ +A_{s2}^* A_{p2} - A_{s2} A_{p2}^* \right\} \hat{\mathbf{p}} \\ \left\{ \begin{array}{l} +\frac{k_{s1}^2 - \kappa^2}{k^2} \frac{k_{p1}}{k} \text{Im} \left[+A_{s1}^* A_{p2} e^{-2ik_{s1}s} - A_{s1} A_{p2}^* e^{+2ik_{s1}s} \right] \\ +A_{s2}^* A_{p1} e^{+2ik_{s1}s} - A_{s2} A_{p1}^* e^{-2ik_{s1}s} \end{array} \right\} \hat{\mathbf{s}} e^{-2\kappa z}, \\ \left\{ \begin{array}{l} -\frac{\kappa^2}{k^2} \frac{k_{s1}}{k} \text{Im} \left[+A_{s1}^* A_{p1} - A_{s1} A_{p1}^* \right] - \frac{\kappa k_{p1}}{k^2} \left[+A_{s1}^* A_{s1} + A_{p1}^* A_{p1} \right] \\ -A_{s2}^* A_{p2} + A_{s2} A_{p2}^* \right\} \hat{\mathbf{s}} \\ \left\{ \begin{array}{l} -\frac{\kappa k_{p1}}{k^2} \left[+A_{s1}^* A_{s2} e^{-2ik_{s1}s} + A_{s2}^* A_{s1} e^{+2ik_{s1}s} \right. \\ \left. +A_{p1}^* A_{p2} e^{-2ik_{s1}s} + A_{p2}^* A_{p1} e^{+2ik_{s1}s} \right] \end{array} \right\} \hat{\mathbf{z}} \end{array} \right\}$$

respectively. There are three components for the vorticity of kinetic momentum, which is attributed to the inhomogeneity of the polarized density in the ps -plane due to the interference, the inhomogeneities of the helical density in the pz -plane and the sz -plane. The discrepancy between the SAM and the vorticity of kinetic momentum is

$$\mathbf{S} - \frac{1}{2k^2} \nabla \times \mathbf{\Pi} = \hbar \sigma_1 \hat{\mathbf{k}}_1 + \hbar \sigma_2 \hat{\mathbf{k}}_2 + \hbar \sigma_c \left[\frac{W_c}{\hbar \omega} \frac{k_{p1}}{k} \hat{\mathbf{p}} \right]. \quad (\text{S.37})$$

with the coupling helix

$$\sigma_c = \frac{\text{Im} \left\{ \left(A_{s1}^* A_{p2} e^{-2ik_{s1}s} - A_{s1} A_{p2}^* e^{2ik_{s1}s} \right) + \left(A_{s2}^* A_{p1} e^{2ik_{s1}s} - A_{s2} A_{p1}^* e^{-2ik_{s1}s} \right) \right\}}{\left(A_{p1}^* A_{p2} e^{-2ik_{s1}s} + A_{p2}^* A_{p1} e^{2ik_{s1}s} \right) + \left(A_{s1}^* A_{s2} e^{-2ik_{s1}s} + A_{s2}^* A_{s1} e^{2ik_{s1}s} \right)}. \quad (\text{S.38})$$

Here, the 1st/2nd term of numerator in Eq. (S.38) is the polarization ellipticity originated from the contribution between the *s/p* component of wave 1 and *p/s* component of wave 2 and the denominator is the coupling energy density (S.34).

On the other hand, considering the interference field, the directional vector of local wave vector is

$$\begin{aligned} \hat{\mathbf{k}} &= \frac{W}{\hbar \omega} \left(\frac{k_{p1}}{k} \hat{\mathbf{p}} + \frac{k_{s1}}{k} \frac{\left(A_{s1}^* A_{s1} + A_{p1}^* A_{p1} - A_{s2}^* A_{s2} - A_{p2}^* A_{p2} \right)}{W} \hat{\mathbf{s}} + 0 \hat{\mathbf{z}} \right) \\ &= \underbrace{\frac{W_1}{\hbar \omega} \left(\frac{k_{p1}}{k} \hat{\mathbf{p}} + \frac{k_{s1}}{k} \hat{\mathbf{s}} + 0 \hat{\mathbf{z}} \right)}_{\hat{\mathbf{k}}_1} + \underbrace{\frac{W_2}{\hbar \omega} \left(\frac{k_{p1}}{k} \hat{\mathbf{p}} - \frac{k_{s1}}{k} \hat{\mathbf{s}} + 0 \hat{\mathbf{z}} \right)}_{\hat{\mathbf{k}}_2} + \underbrace{\frac{W_c}{\hbar \omega} \frac{k_{p1}}{k} \hat{\mathbf{p}}}_{\hat{\mathbf{k}}_c} = \hat{\mathbf{k}}_1 + \hat{\mathbf{k}}_2 + \hat{\mathbf{k}}_c. \end{aligned} \quad (\text{S.39})$$

By checking Eqs. (S.37) and (S.39), we can conclude that the coupling energy density W_c can be considered as propagating along the *p*-direction. In this sense, the integral of this coupling helix σ_c on the whole transverse plane (*sz*-plane) vanishes, which indicates that the helical property of this coupling term is local and does not affect the conservation of total angular momentum. Thus, we can rewrite the Eq. (S.37) as

$$\mathbf{S} - \frac{1}{2k^2} \nabla \times \mathbf{\Pi} = \hbar \sigma_1 \hat{\mathbf{k}}_1 + \hbar \sigma_2 \hat{\mathbf{k}}_2 + \hbar \sigma_c \hat{\mathbf{k}}_c, \quad (\text{S.40})$$

with

$$\hat{\mathbf{k}}_c = \frac{W_c}{\hbar \omega} \frac{k_{p1}}{k} \hat{\mathbf{p}}. \quad (\text{S.41})$$

Interestingly, for a special case that $A_{s1}^* = A_{s2}$ and $A_{p1}^* = A_{p2}$, the coupling helix vanishes. And the Eq. (S.40) can be rewritten as

$$\mathbf{S}_l = \mathbf{S} - \frac{1}{2k^2} \nabla \times \mathbf{\Pi} = \hbar \sigma_1 \hat{\mathbf{k}}_1 + \hbar \sigma_2 \hat{\mathbf{k}}_2. \quad (\text{S.42})$$

Equations (S.40) and (S.42) shows that the difference between the total SAM and the T-spin given by the vorticity of kinetic momentum is the L-spin definitely.

In summary, the spin properties of interferential field between the elliptically polarized evanescent plane waves can be expressed as:

$$\mathbf{S}_l = \hbar \sigma \otimes \hat{\mathbf{k}}, \quad \mathbf{S}_t = \frac{1}{2k^2} \nabla \times \boldsymbol{\Pi} \quad \text{and} \quad \mathbf{S} = \mathbf{S}_l + \mathbf{S}_t. \quad (\text{S.43})$$

Here, the symbol \otimes indicates that the interlink between the EM helices and local wavevectors is local.

Thus, for the generic evanescent waves, the L-spin and T-spin satisfy the relations given by [Eq. 1 and](#) [Eq. 2 of main text](#).

V. Spin properties of interferential propagating plane waves

The former section considers the spin properties of two-waves interference between two evanescent plane waves. Here, we generalize the analysis to the two-waves interference in free space.

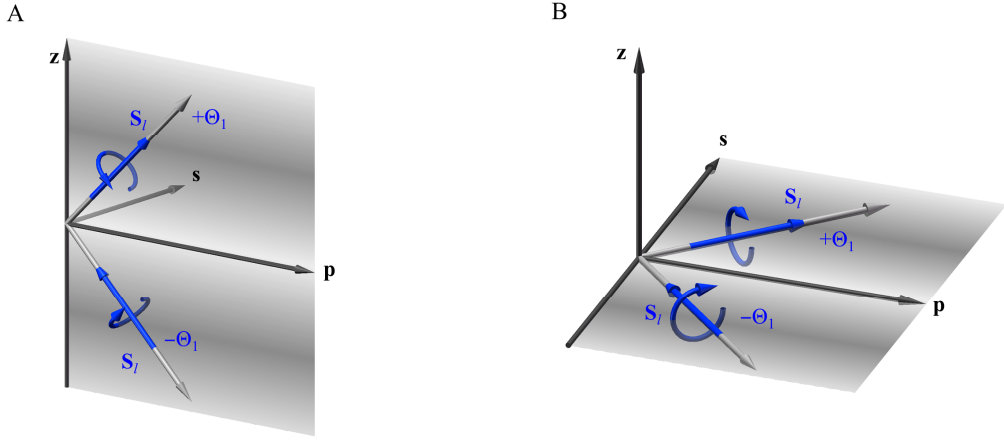


Fig. S5. (A) The schematic diagram of the interference between two elliptically polarized propagating plane waves in pz -plane. The intersected angle between the individual wave and the p -axis is Θ_1 . (B) The schematic diagram of the interference between two elliptically polarized propagating plane waves in ps -plane. The intersected angle between the individual wave and the p -axis is Θ_1 .

We first consider the interference of two propagating plane waves (wave 1: A_{s1}, A_{p1} and wave 2: A_{s2}, A_{p2}) propagating along the zp -plane with an angle $2\Theta_1$ between their wave vectors $\mathbf{k}_{1,2} = k_{p1}\hat{\mathbf{p}} \pm k_{z1}\hat{\mathbf{z}}$ where $k_{p1} = k \cos \Theta_1$ and $k_{z1} = k \sin \Theta_1$ as shown in Fig. S5(A). For each individual plane wave, the energy density, direction of local wave vector, and SAM can be expressed as:

$$W_1 = \frac{\epsilon}{2} \{ A_{s1}^* A_{s1} + A_{p1}^* A_{p1} \}, \quad W_2 = \frac{\epsilon}{2} \{ A_{s2}^* A_{s2} + A_{p2}^* A_{p2} \}, \quad (\text{S.44})$$

$$\hat{\mathbf{k}}_1 = \frac{W_1}{\hbar\omega} \left(k_{p1}/k \hat{\mathbf{p}} + 0 \hat{\mathbf{s}} + k_{z1}/k \hat{\mathbf{z}} \right), \quad \hat{\mathbf{k}}_2 = \frac{W_2}{\hbar\omega} \left(k_{p1}/k \hat{\mathbf{p}} + 0 \hat{\mathbf{s}} - k_{z1}/k \hat{\mathbf{z}} \right), \quad (\text{S.45})$$

and

$$\mathbf{S}_1 = \mathbf{S}_{l,1} = \hbar \frac{\text{Im} \{ A_{s1}^* A_{p1} - A_{p1}^* A_{s1} \}}{A_{s1}^* A_{s1} + A_{p1}^* A_{p1}} \hat{\mathbf{k}}_1 = \hbar \sigma_1 \hat{\mathbf{k}}_1, \quad \mathbf{S}_2 = \mathbf{S}_{l,2} = \hbar \frac{\text{Im} \{ A_{s2}^* A_{p2} - A_{p2}^* A_{s2} \}}{A_{s2}^* A_{s2} + A_{p2}^* A_{p2}} \hat{\mathbf{k}}_2 = \hbar \sigma_2 \hat{\mathbf{k}}_2. \quad (\text{S.46})$$

These results match well with those of Equations (S.9), (S.12) and (S.13).

For the interference field, the energy density is

$$W = \frac{\epsilon}{2} \left\{ \underbrace{A_{s1}^* A_{s1} + A_{p1}^* A_{p1} + A_{s2}^* A_{s2} + A_{p2}^* A_{p2}}_{W_1} + \underbrace{A_{s1}^* A_{s2} + A_{p1}^* A_{p2}}_{W_2} + \underbrace{\frac{k_{p1}^2}{k^2} (A_{s1}^* A_{s2} e^{-2ik_{z1}z} + A_{s2}^* A_{s1} e^{2ik_{z1}z} + A_{p1}^* A_{p2} e^{-2ik_{z1}z} + A_{p2}^* A_{p1} e^{2ik_{z1}z})}_{W_c} \right\} = W_1 + W_2 + W_c, \quad (\text{S.47})$$

The term W_c represents the coupling energy density.

The SAM and the T-spin given by the vorticity of kinetic momentum are

$$\mathbf{S} = \frac{\epsilon}{2\omega} \left\{ \begin{array}{l} \frac{k_{p1}}{k} \text{Im} \left[+ (A_{s1}^* A_{p1} - A_{s1} A_{p1}^*) + (A_{s2}^* A_{p2} - A_{s2} A_{p2}^*) \right] \hat{\mathbf{p}} \\ \frac{k_{p1} k_{z1}}{k^2} \text{Im} \left[+ (A_{s1}^* A_{p2} e^{-2ik_{z1}z} - A_{s1} A_{p2}^* e^{2ik_{z1}z}) + (A_{s2}^* A_{p1} e^{2ik_{z1}z} - A_{s2} A_{p1}^* e^{-2ik_{z1}z}) \right] \hat{\mathbf{s}} \\ \frac{k_{z1}}{k} \text{Im} \left[+ (A_{s1}^* A_{p1} - A_{s1} A_{p1}^*) - (A_{s2}^* A_{p2} - A_{s2} A_{p2}^*) \right] \hat{\mathbf{z}} \end{array} \right\} \quad (\text{S.48})$$

and

$$\mathbf{S}_t = \frac{1}{2k^2} \nabla \times \mathbf{\Pi} = \frac{\epsilon}{2\omega} \text{Im} \left\{ \begin{array}{l} \frac{k_{p1} k_{z1}^2}{k^3} \left[+ (A_{s1}^* A_{p2} e^{-2ik_{z1}z} - A_{s1} A_{p2}^* e^{2ik_{z1}z}) + (A_{s2}^* A_{p1} e^{2ik_{z1}z} - A_{s2} A_{p1}^* e^{-2ik_{z1}z}) \right] \\ \frac{k_{p1} k_{z1}}{k^2} \left[+ (A_{s1}^* A_{s2} e^{-2ik_{z1}z} - A_{s1} A_{s2}^* e^{2ik_{z1}z}) + (A_{p1}^* A_{p2} e^{-2ik_{z1}z} - A_{p2} A_{p1}^* e^{2ik_{z1}z}) \right] \\ 0 \end{array} \right\}, \quad (\text{S.49})$$

respectively. Note that there are two components for the vorticity of kinetic momentum, which is attributed to the inhomogeneity of the polarized density in the pz -plane and the inhomogeneity of the helical density in the sz -plane due to the interference. The discrepancy between the SAM and the vorticity of kinetic momentum is

$$\mathbf{S} - \frac{1}{2k^2} \nabla \times \mathbf{\Pi} = \hbar \sigma_1 \hat{\mathbf{k}}_1 + \hbar \sigma_2 \hat{\mathbf{k}}_2 + \hbar \sigma_c \left[\frac{W_c(\mathbf{r})}{\hbar \omega} \frac{k_{p1}}{k} \hat{\mathbf{p}} \right]. \quad (\text{S.50})$$

with the coupling helix

$$\sigma_c = \frac{\text{Im} \left\{ (A_{s1}^* A_{p2} e^{-2ik_{z1}z} - A_{s1} A_{p2}^* e^{2ik_{z1}z}) + (A_{s2}^* A_{p1} e^{2ik_{z1}z} - A_{s2} A_{p1}^* e^{-2ik_{z1}z}) \right\}}{(A_{p1}^* A_{p2} e^{-2ik_{z1}z} + A_{p2} A_{p1}^* e^{2ik_{z1}z}) + (A_{s1}^* A_{s2} e^{-2ik_{z1}z} + A_{s2} A_{s1}^* e^{2ik_{z1}z})}. \quad (\text{S.51})$$

Here, the 1st/2nd term of numerator in Eq. (S.51) represents the polarization ellipticity between the s/p component of wave 1 and p/s component of wave 2, and the denominator of σ_c is the coupling energy density (S.47).

On the other hand, considering the interference field, the directional vector of local wave vector is

$$\begin{aligned}
\hat{\mathbf{k}} &= \frac{W}{\hbar\omega} \left(+ \frac{k_{p1}}{k} \hat{\mathbf{p}} + 0\hat{\mathbf{s}} + \frac{k_{z1}}{k} \frac{\varepsilon}{2} \frac{(A_{p1}^* A_{p1} + A_{s1}^* A_{s1} - A_{p2}^* A_{p2} - A_{s2}^* A_{s2})}{W} \hat{\mathbf{z}} \right) \\
&= \frac{W_1}{\hbar\omega} \left(+ \frac{k_{p1}}{k} \hat{\mathbf{p}} + 0\hat{\mathbf{s}} + \frac{k_{z1}}{k} \hat{\mathbf{z}} \right) + \frac{W_2}{\hbar\omega} \left(+ \frac{k_{p1}}{k} \hat{\mathbf{p}} + 0\hat{\mathbf{s}} - \frac{k_{z1}}{k} \hat{\mathbf{z}} \right) + \frac{W_c}{\hbar\omega} \frac{k_{p1}}{k} \hat{\mathbf{p}} = \hat{\mathbf{k}}_1 + \hat{\mathbf{k}}_2 + \hat{\mathbf{k}}_c
\end{aligned} \quad . \quad (\text{S.52})$$

Thus, we can rewrite the Equation (S.50) as

$$\mathbf{S} - \frac{1}{2k^2} \nabla \times \mathbf{\Pi} = \hbar\sigma_1 \hat{\mathbf{k}}_1 + \hbar\sigma_2 \hat{\mathbf{k}}_2 + \hbar\sigma_c \hat{\mathbf{k}}_c, \quad (\text{S.53})$$

with

$$\hat{\mathbf{k}}_c = \frac{W_c}{\hbar\omega} \frac{k_{p1}}{k} \hat{\mathbf{p}}. \quad (\text{S.54})$$

For a special case that $A_{s1}^* = A_{s2}$ and $A_{p1}^* = A_{p2}$, the coupling helix σ_c vanishes. The Eq. (S.53) can be

rewritten as

$$\mathbf{S} - \frac{1}{2k^2} \nabla \times \mathbf{\Pi} = \hbar\sigma_1 \hat{\mathbf{k}}_1 + \hbar\sigma_2 \hat{\mathbf{k}}_2. \quad (\text{S.55})$$

Equations (S.53) and (S.55) shows that the difference between the total SAM and the T-spin given by the vorticity of kinetic momentum is the L-spin definitely.

In summary, the spin-momentum properties of interferential field between the elliptically polarized plane waves in pz -plane can be summed as:

$$\mathbf{S}_l = \hbar\sigma \otimes \hat{\mathbf{k}}, \quad \mathbf{S}_t = \frac{1}{2k^2} \nabla \times \mathbf{\Pi} \quad \text{and} \quad \mathbf{S} = \mathbf{S}_l + \mathbf{S}_t. \quad (\text{S.56})$$

Subsequently, as shown in Fig. S5(B), we consider a superposition of two propagating plane waves (wave 1: A_{s1}, A_{p1} and wave 2: A_{s2}, A_{p2}) propagating along ps -plane with an angle $2\Theta_1$ between their wave vectors $\mathbf{k}_{1,2} = k_{p1} \hat{\mathbf{p}} \pm k_{s1} \hat{\mathbf{s}}$ where $k_{p1} = k \cos \Theta_1$ and $k_{s1} = k \sin \Theta_1$. The derivations are similar to the former interference in the pz -plane, we summarize the results briefly. For the individual plane wave, the energy density, direction of local wave vector, and SAM can be expressed as:

$$W_1 = \frac{\varepsilon}{2} \{ A_{p1}^* A_{p1} + A_{s1}^* A_{s1} \}, \quad W_2 = \frac{\varepsilon}{2} \{ A_{p2}^* A_{p2} + A_{s2}^* A_{s2} \}, \quad (\text{S.57})$$

$$\hat{\mathbf{k}}_1 = \frac{W_1}{\hbar\omega} \left(k_{p1}/k \hat{\mathbf{p}} + k_{s1}/k \hat{\mathbf{s}} + 0\hat{\mathbf{z}} \right), \quad \hat{\mathbf{k}}_2 = \frac{W_2}{\hbar\omega} \left(k_{p2}/k \hat{\mathbf{p}} - k_{s1}/k \hat{\mathbf{s}} + 0\hat{\mathbf{z}} \right), \quad (\text{S.58})$$

and

$$\mathbf{S}_1 = \mathbf{S}_{l,1} = \hbar \frac{\text{Im} \{ A_{s1}^* A_{p1} - A_{p1}^* A_{s1} \}}{A_{p1}^* A_{p1} + A_{s1}^* A_{s1}} \hat{\mathbf{k}}_1 = \hbar\sigma_1 \hat{\mathbf{k}}_1, \quad \mathbf{S}_2 = \mathbf{S}_{l,1} = \hbar \frac{\text{Im} \{ A_{s2}^* A_{p2} - A_{p2}^* A_{s2} \}}{A_{p2}^* A_{p2} + A_{s2}^* A_{s2}} \hat{\mathbf{k}}_2 = \hbar\sigma_2 \hat{\mathbf{k}}_2. \quad (\text{S.59})$$

For the interference field, the energy density is

$$W = \frac{\varepsilon}{2} \left\{ \underbrace{A_{p1}^* A_{p1} + A_{s1}^* A_{s1} + A_{p2}^* A_{p2} + A_{s2}^* A_{s2}}_{W_1} + \underbrace{A_{p2}^* A_{p2} + A_{s2}^* A_{s2}}_{W_2} + \underbrace{\frac{k_{p1}^2}{k^2} (A_{p2}^* A_{p1} e^{2ik_{s1}s} + A_{p1}^* A_{p2} e^{-2ik_{s1}s} + A_{s2}^* A_{s1} e^{2ik_{s1}s} + A_{s1}^* A_{s2} e^{-2ik_{s1}s})}_{W_c} \right\} = W_1 + W_2 + W_c, \quad (\text{S.60})$$

with the coupling energy term W_c .

The SAM and the T-spin given by the vorticity of kinetic momentum are

$$\mathbf{S} = \frac{\varepsilon}{2\omega} \text{Im} \left\{ \begin{array}{l} \frac{k_{p1}}{k} \left[+ (A_{s1}^* A_{p1} - A_{s1} A_{p1}^*) + (A_{s2}^* A_{p2} - A_{s2} A_{p2}^*) \right] \hat{\mathbf{p}} \\ \frac{k_{s1}}{k} \left[+ (A_{s1}^* A_{p2} e^{-2ik_{s1}s} - A_{s1} A_{p2}^* e^{2ik_{s1}s}) + (A_{s2}^* A_{p1} e^{2ik_{s1}s} - A_{s2} A_{p1}^* e^{-2ik_{s1}s}) \right] \hat{\mathbf{s}} \\ \frac{k_{s1} k_{p1}}{k^2} \left[- (A_{s1}^* A_{s2} e^{-2ik_{s1}s} - A_{s1} A_{s2}^* e^{2ik_{s1}s}) - (A_{p1}^* A_{p2} e^{-2ik_{s1}s} - A_{p1} A_{p2}^* e^{2ik_{s1}s}) \right] \hat{\mathbf{z}} \end{array} \right\}, \quad (\text{S.61})$$

and

$$\mathbf{S}_t = \frac{1}{2k^2} \nabla \times \mathbf{\Pi} = \frac{\varepsilon}{2\omega} \text{Im} \left\{ \begin{array}{l} \frac{k_{p1} k_{s1}^2}{k^3} \left[A_{s1}^* A_{p2} e^{-2ik_{s1}s} - A_{s1} A_{p2}^* e^{2ik_{s1}s} + A_{s2}^* A_{p1} e^{2ik_{s1}s} - A_{s2} A_{p1}^* e^{-2ik_{s1}s} \right] \hat{\mathbf{p}} \\ 0 \hat{\mathbf{s}} \\ \frac{k_{p1} k_{s1}}{k^2} \left[- A_{s1}^* A_{s2} e^{-2ik_{s1}s} + A_{s1} A_{s2}^* e^{2ik_{s1}s} - A_{p1}^* A_{p2} e^{-2ik_{s1}s} + A_{p1} A_{p2}^* e^{2ik_{s1}s} \right] \hat{\mathbf{z}} \end{array} \right\}, \quad (\text{S.62})$$

respectively. The discrepancy between the SAM and the vorticity of kinetic momentum is

$$\mathbf{S} - \frac{1}{2k^2} \nabla \times \mathbf{\Pi} = \hbar \sigma_1 \hat{\mathbf{k}}_1 + \hbar \sigma_2 \hat{\mathbf{k}}_2 + \hbar \sigma_c \left[\frac{W_c}{\hbar \omega} \frac{k_{p1}}{k} \hat{\mathbf{p}} \right]. \quad (\text{S.63})$$

with the interferential helix

$$\sigma_c = \frac{\text{Im} \left\{ (A_{s1}^* A_{p2} e^{-2ik_{s1}s} - A_{s1} A_{p2}^* e^{2ik_{s1}s}) + (A_{s2}^* A_{p1} e^{2ik_{s1}s} - A_{s2} A_{p1}^* e^{-2ik_{s1}s}) \right\}}{A_{p2}^* A_{p1} e^{2ik_{s1}s} + A_{p1}^* A_{p2} e^{-2ik_{s1}s} + A_{s2}^* A_{s1} e^{2ik_{s1}s} + A_{s1}^* A_{s2} e^{-2ik_{s1}s}}. \quad (\text{S.64})$$

The directional vector of local wave vector of the interference field is

$$\hat{\mathbf{k}} = \frac{W_1}{\hbar \omega} \left(\frac{k_{p1}}{k} \hat{\mathbf{p}} + \frac{k_{s1}}{k} \hat{\mathbf{s}} + 0 \hat{\mathbf{z}} \right) + \frac{W_2}{\hbar \omega} \left(\frac{k_{p1}}{k} \hat{\mathbf{p}} - \frac{k_{s1}}{k} \hat{\mathbf{s}} + 0 \hat{\mathbf{z}} \right) + \frac{W_c}{\hbar \omega} \frac{k_{p1}}{k} \hat{\mathbf{p}} = \hat{\mathbf{k}}_1 + \hat{\mathbf{k}}_2 + \hat{\mathbf{k}}_c. \quad (\text{S.65})$$

The Eq. (S.63) can be rewritten as

$$\mathbf{S} - \frac{1}{2k^2} \nabla \times \mathbf{\Pi} = \hbar \sigma_1 \hat{\mathbf{k}}_1 + \hbar \sigma_2 \hat{\mathbf{k}}_2 + \hbar \sigma_c \hat{\mathbf{k}}_c, \quad (\text{S.66})$$

with directional vector

$$\hat{\mathbf{k}}_c = \frac{W_c}{\hbar \omega} \frac{k_{p1}}{k} \hat{\mathbf{p}}. \quad (\text{S.67})$$

In the case that $A_{s1}^* = A_{s2}$ and $A_{p1}^* = A_{p2}$, the coupling helix σ_c vanishes and the Eq. (S.66) can be

rewritten as

$$\mathbf{S} - \frac{1}{2k^2} \nabla \times \mathbf{\Pi} = \hbar \sigma_1 \hat{\mathbf{k}}_1 + \hbar \sigma_2 \hat{\mathbf{k}}_2. \quad (\text{S.68})$$

Equations (S.66) and (S.68) shows that the difference between the total SAM and the T-spin given by the vorticity of kinetic momentum is the L-spin definitely.

In summary, the spin-momentum properties of interference between the elliptically polarized plane waves in ps -plane can be summed as:

$$\mathbf{S}_l = \hbar \sigma \otimes \hat{\mathbf{k}}, \quad \mathbf{S}_t = \frac{1}{2k^2} \nabla \times \mathbf{\Pi} \quad \text{and} \quad \mathbf{S} = \mathbf{S}_l + \mathbf{S}_t. \quad (\text{S.69})$$

VI. Spin-momentum equations for the generic electromagnetic field

In the former sections, we demonstrate that the T-spin is originated from the transverse inhomogeneities of EM field, while the L-spin is determined by the EM helix solely. By employing the equations (S.5-S.8), we can formulate a novel set of Maxwell-like spin-momentum equations in the uniform nondispersive space as:

$$\nabla \cdot \mathbf{\Pi} = 0, \quad (\text{S.70})$$

$$\nabla \cdot \mathbf{S} = 0, \quad (\text{S.71})$$

$$\nabla \times \mathbf{\Pi} = 2k^2 (\mathbf{S} - \mathbf{S}_l) = 2k^2 \mathbf{S}_l, \quad (\text{S.72})$$

$$\nabla \times \mathbf{S} = 2(\mathbf{\Pi} - \mathbf{P}), \quad (\text{S.73})$$

and the Helmholtz-like equation as

$$\nabla^2 \mathbf{S} + 4k^2 (\mathbf{S} - \mathbf{S}_l) = 2\nabla \times \mathbf{P}. \quad (\text{S.74})$$

VII. Nontrivial spin Chern number of arbitrary structured electromagnetic waves

The photonic spin Chern number for a plane wave was first introduced in Ref. [14]. Here, we give the proof of spin Chern number for an arbitrary structured light akin to the Ref. [14]. The electric/magnetic field can be expressed in the plane-wave basises [S8]

$$\begin{aligned}\mathbf{E}(\mathbf{r}) &= \frac{1}{2\pi} \int_{|\mathbf{k}|=k} \tilde{\mathbf{E}}(\mathbf{k}) e^{i\mathbf{k}\cdot\mathbf{r}} d^2\mathbf{k} \\ \mathbf{H}(\mathbf{r}) &= \frac{1}{2\pi} \int_{|\mathbf{k}|=k} \tilde{\mathbf{H}}(\mathbf{k}) e^{i\mathbf{k}\cdot\mathbf{r}} d^2\mathbf{k}\end{aligned}. \quad (\text{S.75})$$

Transversality constraints in the Maxwell's equations ($\nabla \cdot \mathbf{E} = \nabla \cdot \mathbf{H} = 0$) result in the requirements $\mathbf{k} \cdot \tilde{\mathbf{E}}(\mathbf{k}) = \mathbf{k} \cdot \tilde{\mathbf{H}}(\mathbf{k}) = 0$ for individual plane wave basis, which reduces the EM 3D vector space to the 2D subspace tangential to a sphere in the \mathbf{k} space. However, the AM operators $\hat{\mathbf{L}}$ and $\hat{\mathbf{S}}$ do not keep this subspace invariant. Thus, the total angular momentum operator can be decomposed into two components due to the transversality constraints:

$$\hat{\mathbf{J}} = \hat{\mathbf{L}}' + \hat{\mathbf{S}}' \quad \hat{\mathbf{L}}' = \hat{\mathbf{L}} - \hat{\mathbf{k}} \times (\hat{\mathbf{k}} \times \hat{\mathbf{S}}) \quad \hat{\mathbf{S}}' = \hat{\mathbf{k}} (\hat{\mathbf{k}} \cdot \hat{\mathbf{S}}). \quad (\text{S.76})$$

For the generic structured waves, we choose an auxiliary vector \mathbf{e}_0 and define the other two unit vectors as

$$\mathbf{e}_2 = \frac{\mathbf{e}_0 \times \hat{\mathbf{k}}}{|\mathbf{e}_0 \times \hat{\mathbf{k}}|} \quad \mathbf{e}_1 = \mathbf{e}_2 \times \hat{\mathbf{k}}. \quad (\text{S.77})$$

The unit vectors $(\mathbf{e}_1, \mathbf{e}_2, \hat{\mathbf{k}})$ form an orthogonal frame in which vectors $\tilde{\mathbf{E}}(\mathbf{k})$ and $\tilde{\mathbf{H}}(\mathbf{k})$ lie in the transverse plane $(\mathbf{e}_1, \mathbf{e}_2)$. Next, we introduce the circular polarization basis:

$$\mathbf{e}_+(\mathbf{k}) = \frac{1}{\sqrt{2}}(\mathbf{e}_1 + i\mathbf{e}_2) \quad \mathbf{e}_-(\mathbf{k}) = \frac{1}{\sqrt{2}}(\mathbf{e}_1 - i\mathbf{e}_2), \quad (\text{S.78})$$

in which the plane-wave components of the field can be expressed as

$$\tilde{\mathbf{E}}(\mathbf{k}) = \mathbf{C}_+(\mathbf{k}) + \mathbf{C}_-(\mathbf{k}) \quad (\text{S.79})$$

with $\mathbf{C}_\sigma(\mathbf{k}) = C_\sigma(\mathbf{k}) \mathbf{e}_\sigma(\mathbf{k})$, where $\sigma = \pm 1$ and $C_\sigma(\mathbf{k})$ are the scalar amplitudes of the circularly polarized components. In the novel orthogonal frame, the total angular momentum given by $\mathbf{J} = \int \mathbf{r} \times (\mathbf{p}_s + \mathbf{p}_o) d^2\mathbf{r} = \mathbf{L}' + \mathbf{S}'$ [S9] results in the SAM and OAM components

$$\begin{aligned}\mathbf{S}' &= \frac{\varepsilon}{2\omega} \sum_{\sigma} \int_{|\mathbf{k}|=k} \sigma \hat{\mathbf{k}} |\mathbf{C}_{\sigma}(\mathbf{k})|^2 d^2\mathbf{k} = \frac{\varepsilon}{2\omega} \int_{|\mathbf{k}|=k} \hat{\mathbf{k}} \left[|\mathbf{C}_+(\mathbf{k})|^2 - |\mathbf{C}_-(\mathbf{k})|^2 \right] d^2\mathbf{k} \\ \mathbf{L}' &= \frac{\varepsilon}{2\omega} \sum_{\sigma} \int_{|\mathbf{k}|=k} \mathbf{C}_{\sigma}^*(\mathbf{k}) \cdot \left(-i\mathbf{k} \times \frac{\partial}{\partial \mathbf{k}} - \hat{\mathbf{A}}_B \times \mathbf{k} \right) \mathbf{C}_{\sigma}(\mathbf{k}) d^2\mathbf{k}\end{aligned}. \quad (\text{S.80})$$

By using the Dirac representation and electric–magnetic duality, it can be rewritten as

$$\begin{aligned}\mathbf{S}' &= \left\langle \Psi(\mathbf{k}) \left| \hat{\sigma} \hat{\mathbf{k}} \right| \Psi(\mathbf{k}) \right\rangle \\ \mathbf{L}' &= \left\langle \Psi(\mathbf{k}) \left| \hat{\mathbf{L}} \right| \Psi(\mathbf{k}) \right\rangle - \left\langle \Psi(\mathbf{k}) \left| \sigma \hat{\mathbf{A}}_B \times \mathbf{k} \right| \Psi(\mathbf{k}) \right\rangle\end{aligned}. \quad (\text{S.81})$$

The transformation to the helix basis is associated with the transition to the local coordinate frame with the z axis attached to the \mathbf{k} -vector, which induces pure gauge Coriolis-type potential [S9]

$$\hat{\mathbf{A}}_B = -i\hat{U}^\dagger \partial_{\mathbf{k}} \hat{U}. \quad (\text{S.82})$$

This is the Berry connection, which corresponds to the monopole curvature $\hat{\mathbf{F}}_B = \partial_{\mathbf{k}} \times \hat{\mathbf{A}}_B = \hat{\sigma} \mathbf{k} / k^3$

with $\hat{\sigma} = \text{diag}(1, -1, 0)$ [S9]. From this analysis, the topological Chern numbers for the two helical states can be defined as [14]

$$C^{\sigma} = \frac{1}{2\pi} \int \left\langle \Psi(\mathbf{k}) \left| \hat{\mathbf{F}}_B \right| \Psi(\mathbf{k}) \right\rangle d^2\mathbf{k} = \left\langle \Psi(\mathbf{k}) \left| 2\sigma \right| \Psi(\mathbf{k}) \right\rangle = 2\sigma, \quad (\text{S.83})$$

where the normalization condition, which has the meaning of the number of photons in the wave packet, has a form of $N = \left\langle \Psi(\mathbf{k}) \left| \Psi(\mathbf{k}) \right. \right\rangle = 1$. The spin Chern number is

$$C_{\text{spin}} = \sum_{\sigma=\pm 1} \sigma C^{\sigma} = 4. \quad (\text{S.84})$$

This nontrivial spin Chern number implies that the nontrivial helical states of EM waves indeed exist and are strictly locked to the energy propagation direction. The spin Chern number indicates that there are four helical states locked with the momentum, which are consistent with Fig. S3. Although the transformation between the two helical states is not topologically protected against backscattering, the spin-momentum locking and the induced unidirectional excitation and transportation of photons are the intrinsic feature of the Maxwell's theory and are topological nontrivial (possess \mathbb{Z}_4 topological invariant).

VIII. Transverse spin and Berry curvature

In the section 2, it was mentioned that there is the phase inhomogeneity originated from dynamical propagating phase in the ps -plane or pz -plane as shown in Fig. S1. However, from the derivations in Eq. (S16), no T-spin is generated from the dynamical phase variation. The same conclusion can be reached in the situations exhibited in Fig. S2, Fig. S4 and Fig. S5. Thus, one can conclude that the T-spin is not produced from the dynamical phase. However, is the T-spin related to geometric phase?

First, for the scalar wave in free space or single polarized wave at an optical interface (surface plasmons polaritons [51] or Bloch surface wave [52]), the kinetic momentum can be expressed as the flux density of optical potential [14, 54]. We take the surface plasmons polaritons for example. The kinetic momentum can be expressed as

$$\mathbf{\Pi} = \frac{\varepsilon k^2 k_p^2}{4\omega} \text{Im} \{ \Psi^* \nabla \Psi - \Psi \nabla \Psi^* \} = -\frac{\varepsilon k^2 k_p^2}{2\omega} \langle \Psi | i \nabla | \Psi \rangle. \quad (\text{S.85})$$

Here, Ψ indicates the Hertz potential for transverse magnetic surface modes. Thus, from the Eq. (S.30), the T-spin can be calculated as

$$\mathbf{S}_t = \frac{1}{2k^2} \nabla \times \mathbf{\Pi} = -\frac{\varepsilon k_p^2}{4\omega} \langle \nabla \Psi | \times i | \nabla \Psi \rangle, \quad (\text{S.86})$$

which has a similar form with the Berry curvature of the Hertz potential.

Then, for the generic EM field, through the tedious derivations, one can obtain that

$$\mathbf{S}_t = \frac{1}{2k^2} \nabla \times \mathbf{\Pi} = \frac{\mathbf{S}}{2} - \frac{1}{8\omega^2} \text{Re} \left\{ \begin{array}{l} -(\nabla \odot \mathbf{E}^*) \cdot \mathbf{H} - (\nabla \odot \mathbf{E})^T \cdot \mathbf{H}^* \\ +(\nabla \odot \mathbf{H}^*) \cdot \mathbf{E} + (\nabla \odot \mathbf{H})^T \cdot \mathbf{E}^* \end{array} \right\}, \quad (\text{S.87})$$

where

$$\mathbf{r}_1 \odot \mathbf{r}_2 = \begin{pmatrix} x_i^1 x_i^2 & x_j^1 x_i^2 & x_k^1 x_i^2 \\ x_i^1 x_j^2 & x_j^1 x_j^2 & x_k^1 x_j^2 \\ x_i^1 x_k^2 & x_j^1 x_k^2 & x_k^1 x_k^2 \end{pmatrix}. \quad (\text{S.88})$$

Note that the second part in the right-hand side of Eq. (S.87) has a same structure as the quantum 2-form [S10, S11] that generates the Berry phase associated with a circuit, which indicates a spin-orbit interaction in the optical system. Thus, we can conclude that the T-spin is closely related to the Berry curvature and the evolution of geometric phase in the EM systems.

IX. Spin properties of focusing circular polarization light in free space

To explain the extraordinary properties of L-spin and the spin-momentum and geometric phase-related properties of T-spin, we exhibit the spin properties of focusing circular polarization light. Here, we use Cartesian coordinate (x, y, z) instead of the orthogonal coordinate (p, s, z) . Assuming that the circularly polarized light propagates along z -direction, the electric field of incident light in cylindrical coordinate (ρ, φ, z) systems can be expressed as:

$$\mathbf{E} = \frac{1}{\sqrt{2}} (\hat{\mathbf{e}}_x \pm \sigma i \hat{\mathbf{e}}_y) e^{ikz} = \frac{1}{\sqrt{2}} (e^{\sigma i \varphi} \hat{\mathbf{e}}_\rho + \sigma i e^{\sigma i \varphi} \hat{\mathbf{e}}_\varphi) e^{ikz} = (E_\rho \hat{\mathbf{e}}_\rho + E_\varphi \hat{\mathbf{e}}_\varphi) e^{ikz}. \quad (\text{S.89})$$

Here, $\sigma=\pm 1$ denote the right-handed and left-handed circularly polarized light. From the Richard-Wolf vectorial diffraction theory [S12], the focused electric and magnetic field components can be given by

$$\mathbf{E}_f = \frac{ikf e^{-ikf}}{2\pi} \int_0^{\theta_{\max}} \int_0^{2\pi} \sqrt{\frac{n_i \cos \theta}{n_o}} A(\theta) \begin{pmatrix} \begin{bmatrix} +t_p \cos \theta \cos \varphi E_\rho \\ -t_s \sin \varphi E_\varphi \end{bmatrix} \hat{\mathbf{e}}_x \\ \begin{bmatrix} +t_p \cos \theta \sin \varphi E_\rho \\ +t_s \cos \varphi E_\varphi \end{bmatrix} \hat{\mathbf{e}}_y \\ \begin{bmatrix} -t_p \sin \theta E_\rho \end{bmatrix} \hat{\mathbf{e}}_z \end{pmatrix} \cdot e^{ik[z \cos \theta + r \sin \theta \cos(\varphi - \phi)]} \sin \theta d\varphi d\theta \quad (\text{S.90})$$

and

$$\mathbf{H}_f = \frac{ikf e^{-ikf}}{2\pi\eta} \int_0^{\theta_{\max}} \int_0^{2\pi} \sqrt{\frac{n_i \cos \theta}{n_o}} A(\theta) \begin{pmatrix} \begin{bmatrix} -t_p \sin \varphi E_\rho \\ -t_s \cos \theta \cos \varphi E_\varphi \end{bmatrix} \hat{\mathbf{e}}_x \\ \begin{bmatrix} +t_p \cos \varphi E_\rho \\ -t_s \cos \theta \sin \varphi E_\varphi \end{bmatrix} \hat{\mathbf{e}}_y \\ \begin{bmatrix} +t_s \sin \theta E_\varphi \end{bmatrix} \hat{\mathbf{e}}_z \end{pmatrix} \cdot e^{ik[z \cos \theta + r \sin \theta \cos(\varphi - \phi)]} \sin \theta d\varphi d\theta. \quad (\text{S.91})$$

Here, f is the focal length; n_i and n_o are the refractive indices of incident and focusing plane, respectively; $t_p(\theta)$ and $t_s(\theta)$ are the Fresnel transmission coefficients for p -polarization and s -polarization (we ignore the θ -dependent in the expressions for simplicity.); $\theta=\arcsin(\rho/f)$ and $\theta_{\max}=\arcsin(\text{NA}/n_o)$ with NA denoting the numerical aperture of lens. In the focal plane ($z = 0$), the field components are respectively

$$\mathbf{E}_f = \int_0^{\theta_{\max}} B(\theta) \begin{pmatrix} \{(t_p \cos \theta + t_s) J_0(kr \sin \theta) - (t_p \cos \theta - t_s) J_{2\sigma}(kr \sin \theta)\} e^{\sigma i \varphi} \hat{\mathbf{e}}_r \\ + \sigma i \{(t_p \cos \theta + t_s) J_0(kr \sin \theta) + (t_p \cos \theta - t_s) J_{2\sigma}(kr \sin \theta)\} e^{\sigma i \varphi} \hat{\mathbf{e}}_\varphi \\ \{-2i^\sigma t_p \sin \theta J_\sigma(kr \sin \theta)\} e^{\sigma i \varphi} \hat{\mathbf{e}}_z \end{pmatrix} d\theta, \quad (\text{S.92})$$

$$\mathbf{H}_f = \int_0^{\theta_{\max}} \frac{B(\theta)}{\eta} \begin{pmatrix} -\sigma i \{ (t_p + t_s \cos \theta) J_0(kr \sin \theta) + (t_p - t_s \cos \theta) J_{2\sigma}(kr \sin \theta) \} e^{\sigma i \varphi} \hat{\mathbf{e}}_r \\ \{ (t_p + t_s \cos \theta) J_0(kr \sin \theta) - (t_p - t_s \cos \theta) J_{2\sigma}(kr \sin \theta) \} e^{\sigma i \varphi} \hat{\mathbf{e}}_\phi \\ \{ -2t_s \sin \theta J_\sigma(kr \sin \theta) \} e^{\sigma i \varphi} \hat{\mathbf{e}}_z \end{pmatrix} d\theta. \quad (\text{S.93})$$

Here, $B(\theta) = \frac{ikfe^{-ikf}}{2} A(\theta) \sin \theta \sqrt{\frac{n_i \cos \theta}{2n_o}}$ and J_σ is the σ -order Bessel function of first kind. The detailed

derivations are not given here due to the complexity of the expressions. The z -component SAM is

$$S_z = \hbar \sigma C(r) \quad (\text{S.94})$$

with

$$C(r) = \int_0^{\theta_{\max}} \int_0^{\theta_{\max}} \operatorname{Re} \left[\frac{\varepsilon B_1^* B_2}{2\hbar\omega} \right] \begin{pmatrix} + (t_{s,1} + t_{p,1} \cos \theta_1) (t_{s,2} + t_{p,2} \cos \theta_2) J_0(kr \sin \theta_1) J_0(kr \sin \theta_2) \\ + (t_{p,1} + t_{s,1} \cos \theta_1) (t_{p,2} + t_{s,2} \cos \theta_2) J_0(kr \sin \theta_1) J_0(kr \sin \theta_2) \\ - (t_{s,1} - t_{p,1} \cos \theta_1) (t_{s,2} - t_{p,2} \cos \theta_2) J_2(kr \sin \theta_1) J_2(kr \sin \theta_2) \\ - (t_{p,1} - t_{s,1} \cos \theta_1) (t_{p,2} - t_{s,2} \cos \theta_2) J_2(kr \sin \theta_1) J_2(kr \sin \theta_2) \end{pmatrix} d\theta_1 d\theta_2.$$

Here, the subscripts 1 and 2 represent the different integral quantities. Since the coefficient $C(r)$ is helix-independent, it can be concluded that the z -component SAM is helix-dependent.

On the other hand, the z -component of vorticity of kinetic momentum is

$$S_{t,z} = \left(\frac{1}{2k^2} \nabla \times \mathbf{H} \right)_z = \hbar \sigma D(r) \quad (\text{S.95})$$

with

$$D(r) = \int_0^{\theta_{\max}} \int_0^{\theta_{\max}} \operatorname{Re} \left[\frac{\varepsilon B_1^* B_2}{2\hbar\omega} \right] \begin{pmatrix} + \sin \theta_2 \sin \theta_1 [t_{s,1} t_{s,2} + t_{p,1} t_{s,2} \cos \theta_1] J_0(kr \sin \theta_1) J_0(kr \sin \theta_2) \\ + \sin \theta_1 \sin \theta_2 [t_{p,1} t_{p,2} + t_{p,1} t_{s,2} \cos \theta_2] J_0(kr \sin \theta_1) J_0(kr \sin \theta_2) \\ - \sin \theta_1 \sin \theta_2 [t_{s,1} t_{s,2} + t_{p,1} t_{s,2} \cos \theta_1] J_1(kr \sin \theta_1) J_1(kr \sin \theta_2) \\ - \sin \theta_1 \sin \theta_2 [t_{p,1} t_{p,2} + t_{p,1} t_{s,2} \cos \theta_2] J_1(kr \sin \theta_1) J_1(kr \sin \theta_2) \\ + \sin \theta_1 \sin \theta_1 [t_{p,1} t_{p,2} - t_{p,1} t_{s,2} \cos \theta_2] J_0(kr \sin \theta_1) J_2(kr \sin \theta_2) \\ + \sin \theta_1 \sin \theta_2 [t_{p,1} t_{p,2} - t_{p,1} t_{s,2} \cos \theta_2] J_1(kr \sin \theta_1) J_2(kr \sin \theta_2) \\ + \sin \theta_2 \sin \theta_2 [t_{s,1} t_{s,2} - t_{p,1} t_{s,2} \cos \theta_1] J_2(kr \sin \theta_1) J_0(kr \sin \theta_2) \\ + \sin \theta_1 \sin \theta_2 [t_{s,1} t_{s,2} - t_{p,1} t_{s,2} \cos \theta_1] J_2(kr \sin \theta_1) J_1(kr \sin \theta_2) \end{pmatrix} d\theta_1 d\theta_2.$$

This T-spin is originated from the amplitude and the helical inhomogeneities of focused circular polarization waves. Obviously, $D(r)$ is non-zero, which indicate a helix-dependent T-spin. Thus, we can conclude that the difference between the z -components of SAM and the vorticity of kinetic momentum is the helix-dependent L-spin:

$$\mathbf{S}_{l,z} = \left(\mathbf{S} - \frac{1}{2k^2} \nabla \times \mathbf{H} \right)_z = \hbar \sigma [C(r) - D(r)]. \quad (\text{S.96})$$

Subsequently, from the derivations, we find that the azimuthal T-spin is

$$\left(\frac{1}{2\omega^2} \nabla \times \mathbf{P} \right)_\phi = \int_0^{\theta_{\max}} \int_0^{\theta_{\max}} \operatorname{Re} \left[\frac{\varepsilon B_1^* B_2}{2\omega} \right] \begin{cases} +\sin \theta_1 [t_{p,1} \cos \theta_1 + t_{s,1}] [t_{p,2} + t_{s,2} \cos \theta_2] J_1(kr \sin \theta_1) J_0(kr \sin \theta_2) \\ +\sin \theta_2 [t_{p,1} \cos \theta_1 + t_{s,1}] [t_{p,2} + t_{s,2} \cos \theta_2] J_0(kr \sin \theta_1) J_1(kr \sin \theta_2) \\ -\sin \theta_1 [t_{p,1} \cos \theta_1 - t_{s,1}] [t_{p,2} - t_{s,2} \cos \theta_2] J'_2(kr \sin \theta_1) J_2(kr \sin \theta_2) \\ -\sin \theta_2 [t_{p,1} \cos \theta_1 - t_{s,1}] [t_{p,2} - t_{s,2} \cos \theta_2] J_2(kr \sin \theta_1) J'_2(kr \sin \theta_2) \end{cases} d\theta_1 d\theta_2. \quad (\text{S.97})$$

Equation (S.97) indicates that the azimuthal component of T-spin is helix-independent. This component is regarded as the helix-independent T-spin and is perpendicular to the optical axis. It is worth noting that there is coupling term (given by the multiplying of t_p and t_s) in the azimuthal SAM, and hence the distinction between the azimuthal SAM and azimuthal T-spin is

$$\left(\mathbf{S} - \frac{1}{2\omega^2} \nabla \times \mathbf{P} \right)_\phi \approx \int_0^{\theta_{\max}} \int_0^{\theta_{\max}} \operatorname{Re} \left[\frac{\varepsilon B_1^* B_2}{2\omega} \right] \begin{cases} +\sin \theta_2 [t_{p,1} t_{s,2} (1 - \cos \theta_1 \cos \theta_2) + t_{s,1} t_{s,2} (\cos \theta_1 - \cos \theta_2)] J_0(kr \sin \theta_1) J_1(kr \sin \theta_2) \\ +\sin \theta_1 [t_{p,1} t_{s,2} (1 - \cos \theta_1 \cos \theta_2) - t_{p,1} t_{p,2} (\cos \theta_1 - \cos \theta_2)] J_1(kr \sin \theta_1) J_0(kr \sin \theta_2) \\ +\sin \theta_1 [t_{p,1} t_{s,2} (1 - \cos \theta_1 \cos \theta_2) + t_{p,1} t_{p,2} (\cos \theta_1 - \cos \theta_2)] J_1(kr \sin \theta_1) J_2(kr \sin \theta_2) \\ +\sin \theta_2 [t_{p,1} t_{s,2} (1 - \cos \theta_1 \cos \theta_2) - t_{s,1} t_{s,2} (\cos \theta_1 - \cos \theta_2)] J_2(kr \sin \theta_1) J_1(kr \sin \theta_2) \end{cases} d\theta_1 d\theta_2. \quad (\text{S.98})$$

Although this coupling term is much smaller than the azimuthal T-spin, it should be regarded as the L-spin [S13], which is related to the symmetry of modes. Noteworthily, the terms of the second row in the integration can be cancelled by considering the symmetry.

In addition, it can be deduced that

$$S_r = \left(\frac{1}{2k^2} \nabla \times \mathbf{P} \right)_r = 0. \quad (\text{S.99})$$

This is reasonable since there is no intensity inhomogeneity in the radial direction.

We compare the components of SAM and the T-spin given by the vorticity of kinetic momentum in Fig. S6. The x -component of SAMs [Fig. S6(A) and Fig. S6(F)] and y -component of SAMs [Fig. S6(B) and Fig. S6(G)] are helix-independent, while the z -component SAMs [Fig. S6(C) and Fig. S6(H)] are helix-dependent. There will always be an inverted L-spin exist owing to the geometric phase in the focusing system [S11], albeit this inverted component is much small in the focusing circular polarization lights of free space. Remarkably, the z -component T-spins [Fig. S6(D) and Fig. S6(I)] can be antiparallel to the spin vector of incident wave. By subtracting the z -component T-spins from z -component SAM, the

remaining spins are purely parallel to the spin vector of incident wave (without antiparallel component) [Fig. S1(E) and Fig. S1(J)], which are definitely the L-spins. This phenomenon indicates the T-spin is related to the evolution of geometric phase. The Fig. S7 exhibit the similar phenomena by changing the numerical aperture (NA) to 0.7.

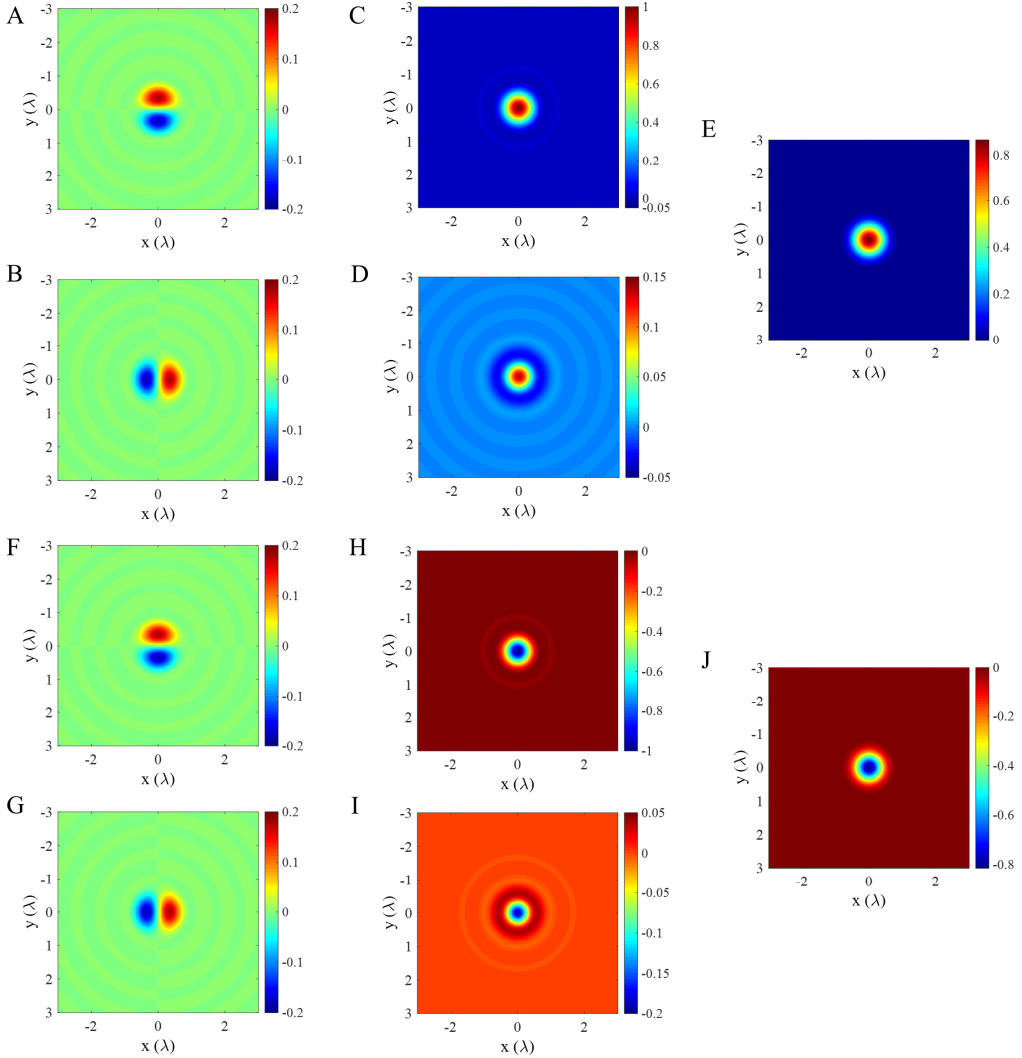


Fig. S6. The spin properties of focused circular polarization lights. The (A) S_x and (B) S_y , (C) S_z , (D) z -component of T-spin and (E) L-spin of the focused right-handed circular polarization light. The (F) S_x and (G) S_y , (H) S_z , (I) z -component of T-spin and (J) L-spin of focused left-handed circular polarization light. From (A), (B), (F) and (G), it can be found that the T-spins are locked with the propagating direction and helix-independent. The L-spin is helix-dependent and inverse as the incident circular polarization is inverted, and the z -component T-spins are also helix-dependent from (D) and (I). Importantly, the inverted SAM components in L-spins disappear in (E) and (J) by subtracting the total spins from T-spins, which are related to the geometric phase. The NA is 0.5 and the wavelength is 632.8nm.

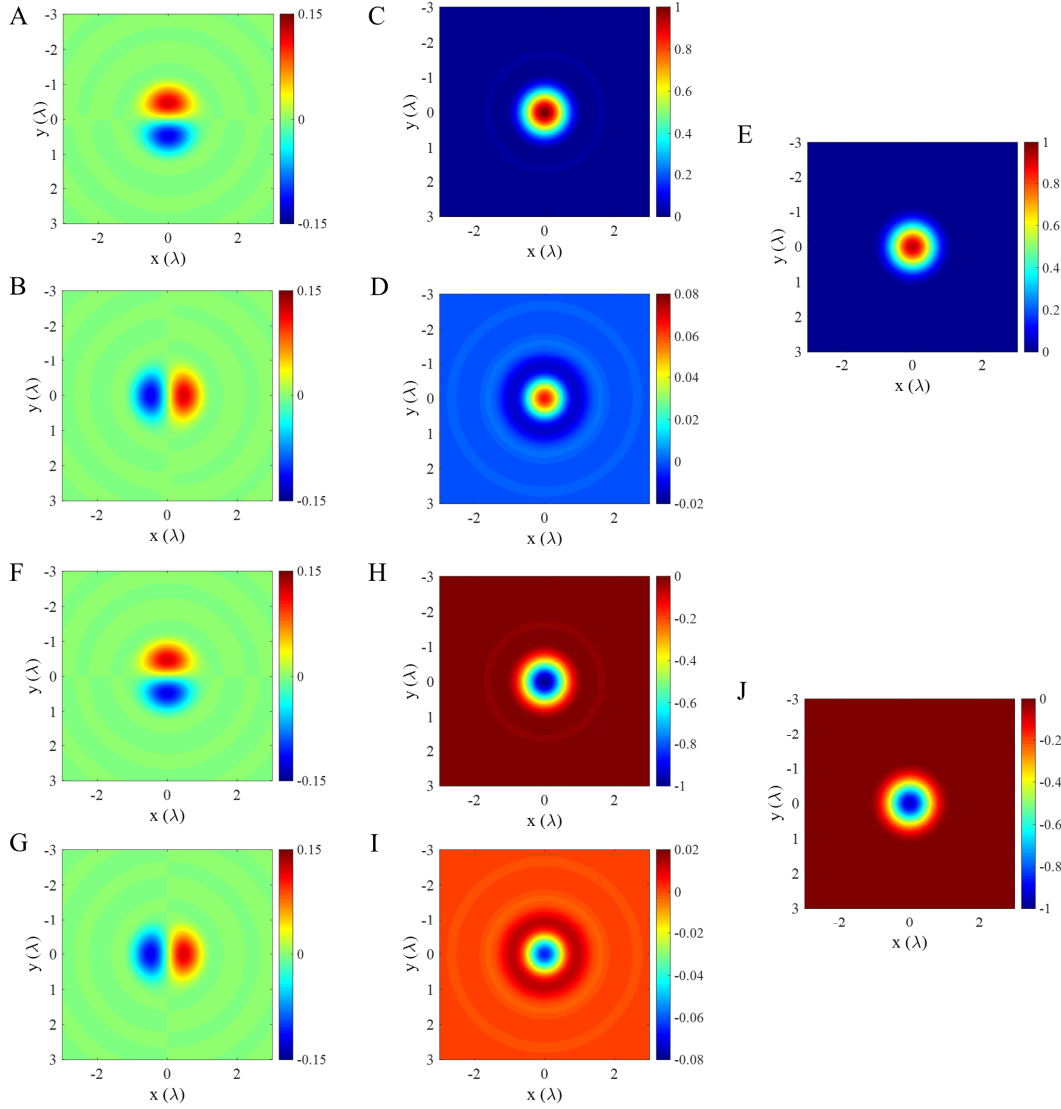


Fig. S7. The spin properties of focused circular polarization lights. The (A) S_x and (B) S_y , (C) S_z , (D) z -component of T-spin and (E) L-spin of the focused right-handed circular polarization light. The (F) S_x and (G) S_y , (H) S_z , (I) z -component of T-spin and (J) L-spin of focused left-handed circular polarization light. From (A), (B), (F) and (G), it can be found that the T-spins are locked with the propagating direction and helix-independent. The L-spin is helix-dependent and inverse as the incident circular polarization is inverted, and the z -component T-spins are also helix-dependent from (D) and (I). Importantly, the inverted SAM components in L-spins disappear in (E) and (J) by subtracting the total spins from T-spins, which are related to the geometric phase. Remarkably, these two situations are corresponding to the two spin-momentum locking states in [Fig. S3\(A\)](#) and [Fig. S3\(C\)](#). Together with the other two states by flipping the propagating direction, the four spin-momentum locking states are consistent with the \mathbb{Z}_4 topological invariant of generic EM modes. The NA is 0.7 and the wavelength is 632.8nm.

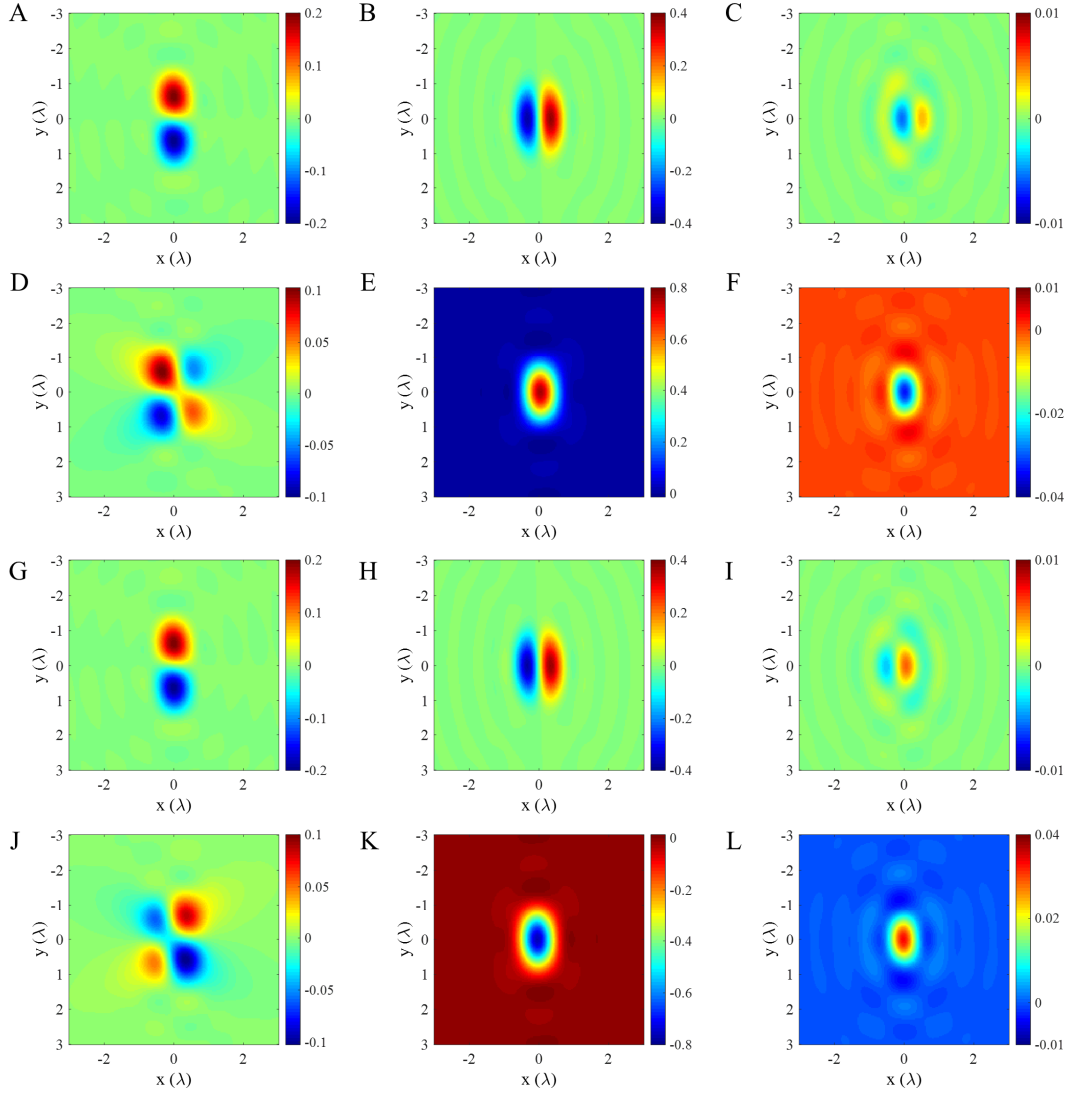


Fig. S8. The spin properties of focused modulated circular polarization lights. The T-spins (A) S_{tx} , (B) S_{ty} , (C) S_{tz} , and the L-spins (D) S_{bx} , (E) S_{by} , (F) S_{bz} , for the focusing of modulated circular polarization light. The incident modulated circular polarization light is constructed by the right-handed circular polarization light in the region $x>0$ and the left-handed circular polarization light in the region $x<0$. The T-spins (G) S_{bx} , (H) S_{by} , (I) S_{bz} , and the L-spins (J) S_{bx} , (K) S_{by} , (L) S_{bz} , for the focusing of inverse modulated circular polarization light. The incident inverse modulated circular polarization light is constructed by the left-handed circular polarization light in the region $x>0$ and the right-handed circular polarization light in the region $x<0$. The T-spins are unchanged and satisfy the spin-momentum locking property, whereas the L-spins are helix-dependent and can be along an arbitrary direction. The slight distinction between (C) and (I) is owing to the helix-dependent property of T-spin in the z-direction. The NA is 0.7 and the wavelength is 632.8nm.

In conclusion, the former results indicate that there are the extraordinary helix-dependent T-spin in the z -direction and the helix-independent T-spin in the azimuthal direction in the focusing of circularly polarized lights. Thus, the spin-momentum locking property of the focused field for the circularly polarized lights is also helix-dependent. Remarkably, these two situations are corresponding to the two spin-momentum locking states in [Fig. S3\(A\)](#) and [Fig. S3\(C\)](#). Together with the other two states by flipping the propagating direction, the four spin-momentum locking states are consistent with the \mathbb{Z}_4 topological invariant of generic EM modes.

Finally, we will show an example akin to the two-wave interference by modulating the circular polarization of incident light. The details can be found in [Fig. S8](#). As the incident helix is inverted, the x and y component of T-spins, which are helix-independent, remain unchanged. Whereas the z component T-spin, which is helix-dependent, varies slightly. These T-spins satisfy the property of spin-momentum locking universally. On the other hand, the L-spins are opposite universally due to the helix-dependent property. In addition, this L-spin is mainly along the transverse direction, which demonstrates an extraordinary property of L-spin.

X. Experimental setup and measurement of SAM perpendicular to optical axis

The experimental setup of the mapping the transverse components of SAM is given in [Fig. S9](#). The incident beam of 632.8nm-wavelength is tightly focused by an objective lens (Olympus, NA=0.5, 50 \times) to a PS nanoparticle with diameter 201nm sitting on a silver film (thickness: 45nm). The focusing field and the scattering field of the PS particle (the far-field radiation field and part of the near-field evanescent field) radiate downward through the coupling of the silver film. Then the signal is collected by an oil immersion objective lens (Olympus, NA = 1.49, 100 \times). By a piezo-stage (Physik Instrumente, P-545), we move precisely the PS particle through the focal plane of a tightly focused beam. Each time the position is moved, the back focal plane intensity (far-field intensity) distribution is imaged by a four-quadrant detector. Through the dipole theory [[S12](#)] and similar techniques as reference [[S14](#)], the transverse components of SAM can be reconstructed.

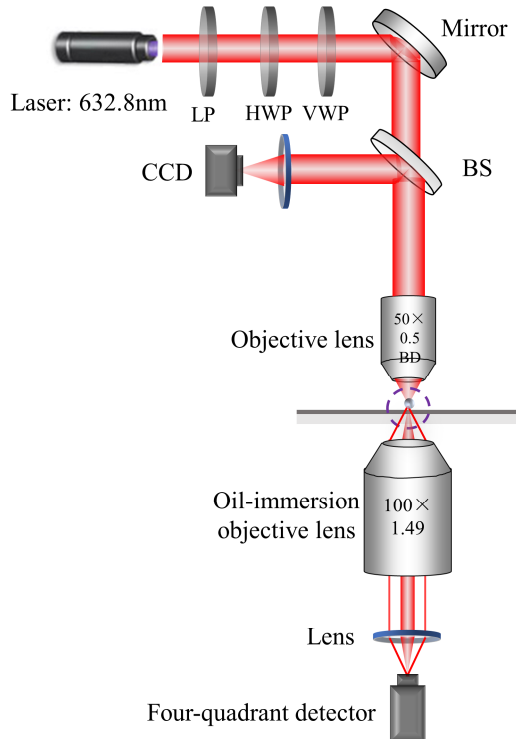


Fig. S9. The schematic diagram for mapping the spin component perpendicular to the optical axis. **LP:** linear polarizer; **HWP:** Half-wave plate; **QWP:** quarter-wave plate; **BS:** unpolarized beam-splitter.

The theoretical and reconstructed results for the focused left-handed circularly polarized light and right-handed circularly polarized light can be found in [Figs. S10 and S11](#). These experimental results match well with the theoretical results, which reveals the helix-independent T-spin in the focusing.

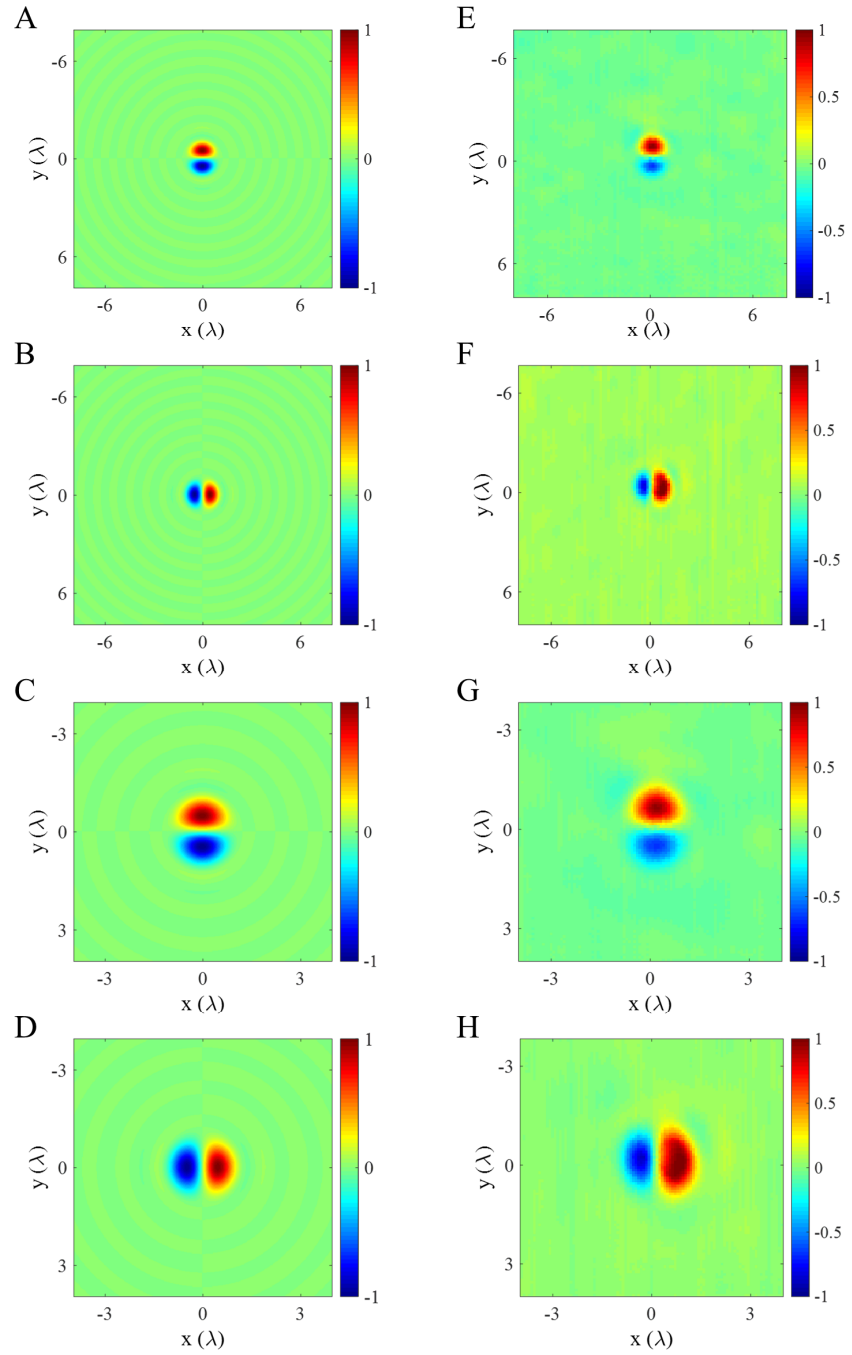


Fig. S10. The theoretical (A) S_x and (B) S_y , and the experimental (E) S_x and (F) S_y for the focused left-handed circularly polarized light in a region of $10\mu\text{m} \times 10\mu\text{m}$. The grid size is 100nm here. The theoretical (C) S_x and (D) S_y , and the experimental (G) S_x and (H) S_y for the focused left-handed circularly polarized light in a region of $5\mu\text{m} \times 5\mu\text{m}$. The grid size is 50nm here. The theoretical results match well with the experimental results. The wavelength is 632.8nm and the numerical aperture is 0.5.

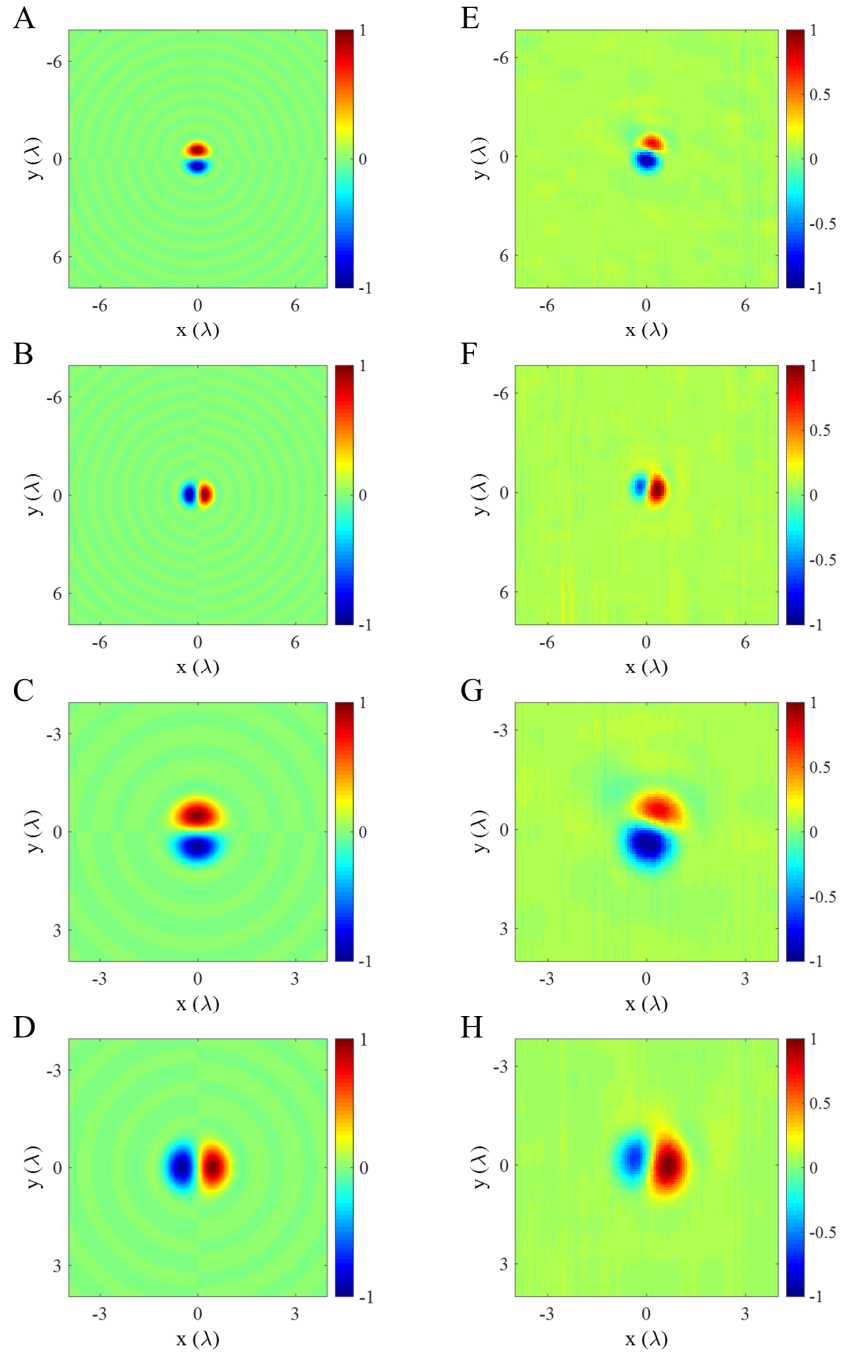


Fig. S11. The theoretical (A) S_x and (B) S_y , and the experimental (E) S_x and (F) S_y for the focused right-handed circularly polarized light in a region of $10\mu\text{m} \times 10\mu\text{m}$. The grid size is 100nm here. The theoretical (C) S_x and (D) S_y , and the experimental (G) S_x and (H) S_y for the focused left-handed circularly polarized light in a region of $5\mu\text{m} \times 5\mu\text{m}$. The grid size is 50nm here. The theoretical results match well with the experimental results. The wavelength is 632.8nm and the numerical aperture is 0.5.

XI. Experimental setup and measurement of SAM parallel to optical axis

The setup of the tip-fiber-based-measurement system to map the out-of-plane component of SAM is shown in [Fig. S12\(a\)](#). A He–Ne laser with an operating wavelength of 632.8 nm was used as a light source. The light beam was expanded and collimated via a telescope system. Then it passed through a linear polarizer (LP) and a quarter wave plate (QWP) to produce the desired left-handed or right-handed circularly polarized lights, which was then focused using an objective lens (Olympus, NA 0.7, 60 \times) onto a silica coverslip properly for the further scanning imaging by a self-assembly near-field scanning optical microscopic (NSOM) system. The NSOM probe with a hole as shown in [Fig. S12\(b\)](#) was controlled using a tuning fork feedback system for mapping of the in-plane field distributions of the focused beams. The near-field signal that was coupled through the nanohole to the fiber was split and then analyzed using a combination of a quarter-wave plate and a linear polarizer to extract the individual circular polarization (I_{LCP} : left-handed circularly polarized component and I_{RCP} : right-handed circularly polarized component) component of the signal. These components were then directed to two photomultiplier tubes (PMTs) to measure the intensity information of the two signals. This then enables characterization of the out-of-plane SAM component (i.e., along the optical axis) of the focused beams by the relation [[S15](#)]:

$$S_z = \frac{\varepsilon}{4\omega} \frac{k^2 + \kappa^2}{\kappa^2} (I_{\text{RCP}} - I_{\text{LCP}}). \quad (\text{S.100})$$

The measured field components and reconstructed out-of-plane SAM can be found in [Fig. S13](#) and [Fig. S14](#) for the right-handed circularly polarized light and left-handed circularly polarized light, respectively. The experimental results match well with the theoretical results, indicating that the L-spin of focused field is inverse as the polarization of incident light switches from the right-handed circular polarization to the left-handed circular polarization. Because there are longitudinal parts of ‘T-spins’ existing in these focused fields, these results can be regarded as the evidences that the T-spin is helix-dependent. The distinctions between the theoretical results and measured results are owing to the three reasons: first, the radius of air-hole is about 50nm, and thus each pixel would collect the light at a region of 100nm \times 100nm. This will downgrade the contrast of image and raise up the intensity of sidelobes; second, although the aperture-type NSOM will collect the transverse components of optical field primarily. However, the longitudinal component can also pass through the air-hole and affect the distributions of measured results; third, it can hardly put the nanoprobe at the focal plane exactly, and thus the scale of focal point at an out-of-focus plane would be larger compared to that of focal plane.

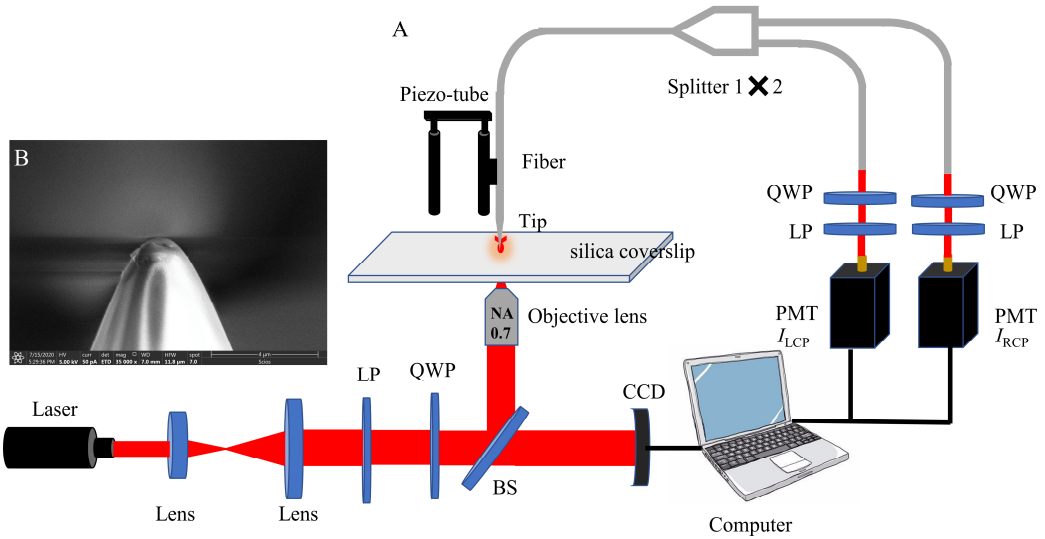


Fig. S12. (a) The schematic diagram for mapping the spin component along the optical axis. The details of experimental method can be found in Ref. [S15]. **LP**: linear polarizer; **QWP**: quarter-wave plate; **PMT**: photo-multiplier tube; **BS**: unpolarized beam-splitter. (b) The scanning electron microscope image of optical fiber nanoprobe with a circular hole. The radius of hole is about 50nm.

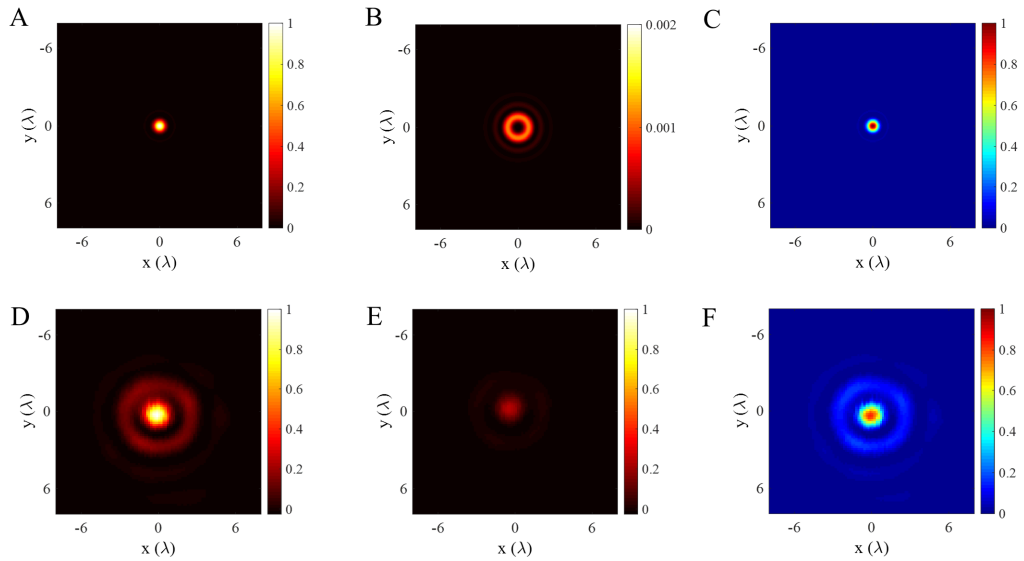


Fig. S13. The theoretical (A) I_{RCP} , (B) I_{LCP} (C) out-of-plane SAM and measured (D) I_{RCP} , (E) I_{LCP} and (F) out-of-plane SAM for the focused right-handed circularly polarized light. The numerical apertures of theoretical and experimental systems are 0.7. The dimension of a pixel is 100nm and the scanned region is $10\mu\text{m} \times 10\mu\text{m}$. Note here that the I_{LCP} is much smaller than the I_{RCP} .

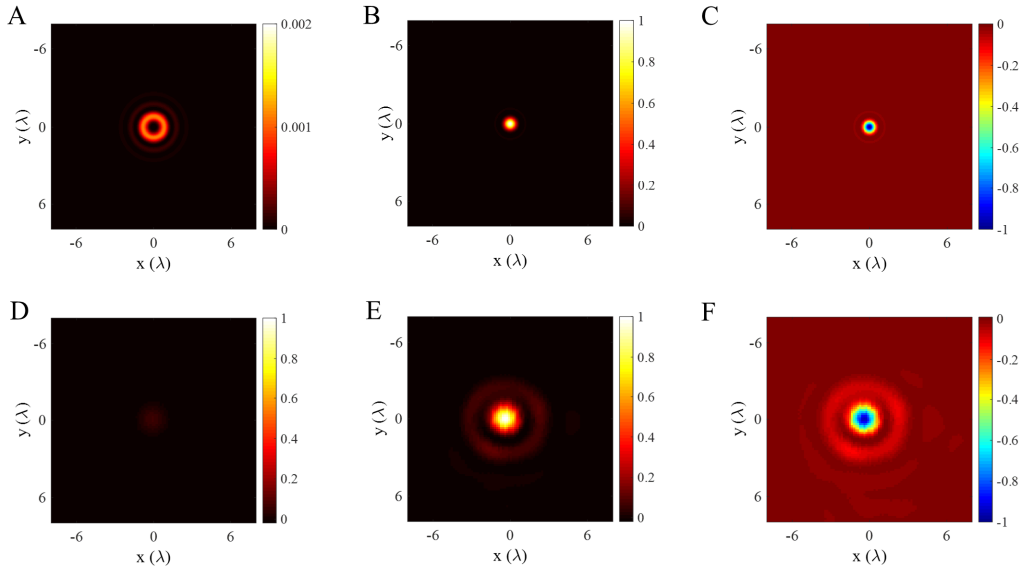


Fig. S14. The theoretical (A) I_{RCP} , (B) I_{LCP} (C) out-of-plane SAM and measured (D) I_{RCP} , (E) I_{LCP} and (F) out-of-plane SAM for the focused left-handed circularly polarized light. The numerical apertures of theoretical and experimental systems are 0.7. The dimension of a pixel is 100nm and the scanned region is $10\mu\text{m} \times 10\mu\text{m}$. Note here that the I_{RCP} is much smaller than the I_{LCP} .

XII. Transverse optical forces by spin-momentum locked photonic skyrmions

In the former analysis, one can realize that the SAMs of the focused circularly polarized lights are similar to the distributions of Bloch-type magnetic skyrmion [S16]. The one-dimensional contours of S_z (red line), S_φ (blue line) and S_r (green dotted line) and vectorgraphs for the focused RCP light and focused LCP light can be found in Fig. S15. The spin vectors vary from ‘up’ state to ‘down’ state for focused RCP light, while the tendency is reversal as the circular polarization of incident wave is inverted.

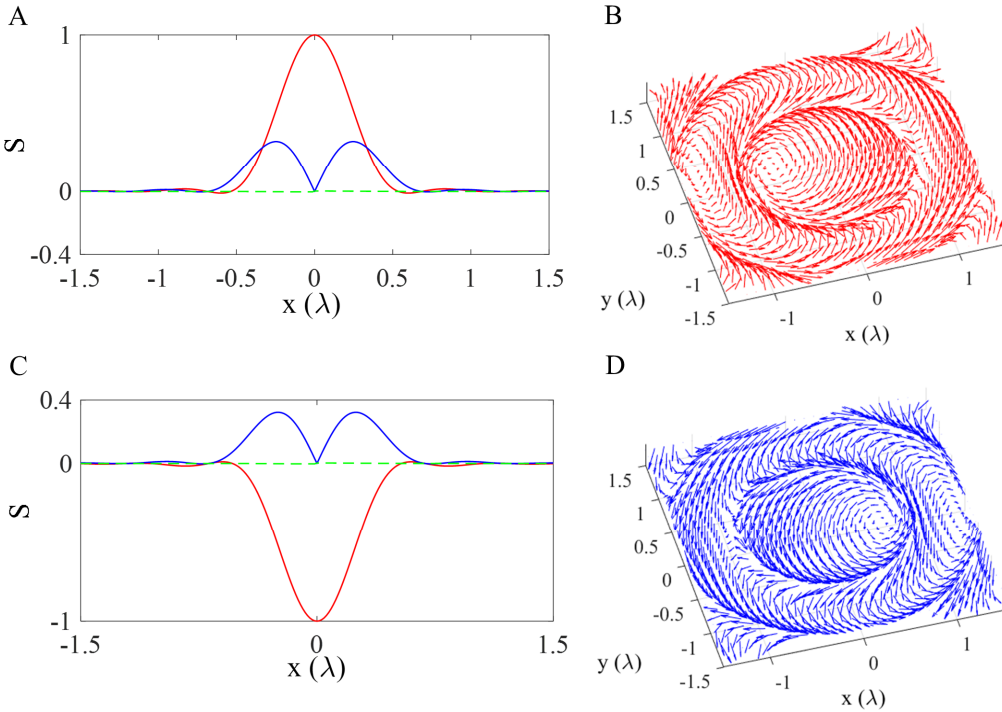


Fig. S15. The spin texture of focused circular polarization lights. (A) The one-dimensional contours of S_z (red line), S_φ (blue line) and S_r (green dotted line) and (B) vectorgraphs for the focused RCP light; (C) the one-dimensional contours of S_z (red line), S_φ (blue line) and S_r (green dotted line) and (D) vectorgraphs for the focused LCP light. The SAMs of the focused circularly polarized lights are similar to the distributions of Bloch-type skyrmion.

In the following, we will give an example for the application of optical spin-momentum locking in free space: the spin-momentum locked transverse optical force for the wideband chiral sorting. The schematic diagram can be found in Fig. S16. The Bloch-type skyrmion with skyrmion number -1 (generated by focused RCP light as shown in Fig. S16(A)) can produce the negative transverse optical force F_x as shown in Fig. S16(B), while the Bloch-type skyrmion with skyrmion number $+1$ (generated by focused LCP light as shown in Fig. S16(F)) can produce positive transverse optical force F_x as shown

in Fig. S16(G). The momentum locked wideband unidirectional optical force can be definitely found in the wavelength region ($\sim 0.8\mu\text{m}$ – $1.2\mu\text{m}$) in the green dotted boxes.

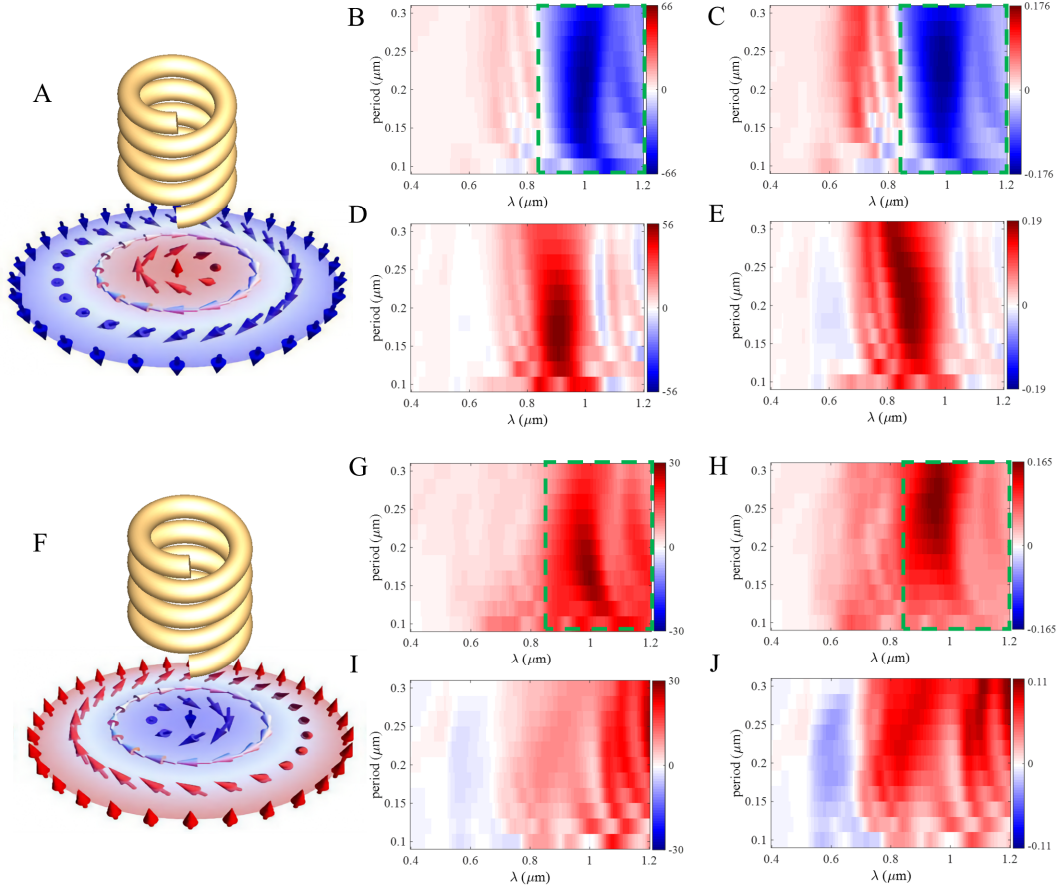


Fig. S16. (A) The schematic diagram of -1 -order optical Bloch-type skyrmion interacting with the gold helix. (B) The transverse optical force F_x and (C) the ratio between the F_x and longitudinal optical force F_z ; (D) The transverse optical force F_y and (E) the ratio between the F_y and longitudinal optical force F_z . (F) The schematic diagram of $+1$ -order optical Bloch-type skyrmion interacting with the gold helix. (G) The transverse optical force F_x and (H) the ratio between the F_x and longitudinal optical force F_z ; (I) The transverse optical force F_y and (J) the ratio between the F_y and longitudinal optical force F_z . The units for (B), (D), (G) and (I) are $10^{-5}\text{pN}\cdot\text{mW}^{-1}\cdot\mu\text{m}^2$. The radius of helix in xy -plane is $0.2\mu\text{m}$; the radius of metal fiber in helix is $0.04\mu\text{m}$; and 4 periods are used here.

Reference:

- [S1] M. V. Berry, Optical currents, *J. Opt. Pure Appl. Opt.* 11(9), 094001 (2009).
- [S2] M. V. Berry and Pragya Shukla, Geometry of 3D monochromatic light: local wavevectors, phases,

curl forces, and superoscillations, *J. Opt.* **21**, 064002 (2019).

[S3] Stephen M. Barnett, Optical Dirac equation, *New Journal of Physics* **16**, 093008 (2014).

[S4] I. Bialynicki-Birula and Z. Bialynicka-Birula, The role of the Riemann–Silberstein vector in classical and quantum theories of electromagnetism, *J. Phys. A: Math. Theor.* **46**, 053001 (2013).

[S5] Deng Pan, Hong Wei, Long Gao, and Hongxing Xu, Strong spin-orbit interaction of light in plasmonic nanostructures and nanocircuits, *Phys. Rev. Lett.* **117**, 166803 (2016).

[S6] Konstantin Y. Bliokh, Aleksandr Y. Bekshaev, and Franco Nori, Optical Momentum, Spin, and Angular Momentum in Dispersive Media, *Phys. Rev. Lett.* **119**, 073901 (2017).

[S7] F. Alpeggiani, K. Y. Bliokh, F. Nori, and L. Kuipers, Electromagnetic helicity in complex media, *Phys. Rev. Lett.* **120**, 243605:1–6 (2018).

[S8] Chun-Fang Li, Spin and orbital angular momentum of a class of nonparaxial light beams having a globally defined polarization, *Phys. Rev. A* **80**, 063814 (2009).

[S9] K. Y. Bliokh, Miguel A. Alonso, Elena A. Ostrovskaya, and A. Aiello, Angular momenta and spin-orbit interaction of nonparaxial light in free space, *Phys. Rev. A* **82**, 063825:1-7 (2010).

[S10] M. V. Berry and M. R. Dennis, Polarization singularities in isotropic random vector waves, *Proc. R. Soc. A* **457**, 141 (2001).

[S11] Berry, M. V., Quantal phase factors accompanying adiabatic changes, *Proc. R. Soc. A* **392**, 45 (1984).

[S12] L. Novotny, B. Hecht and O. Keller, *Principles of nano-optics*, Cambridge University Press, 2012.

[S13] P. Shi, X. Lei, Q. Zhang, H. Li, L. Du, and X. Yuan, Intrinsic spin-momentum dynamics of surface electromagnetic waves in complex dispersive system, *arXiv:2202.09007* (2022).

[S14] M. Neugebauer, J. S. Eismann, T. Bauer, and P. Banzer, Magnetic and electric transverse spin density of spatially confined light, *Phys. Rev. X* **8**, 021042 (2018).

[S15] X. Yin, P. Shi, L. Du, and X.-C. Yuan, Spin-resolved near-field scanning optical microscopy for mapping of the spin angular momentum distribution of focused beams. *Appl. Phys. Lett.* **116**, 241107 (2020).

[S16] N. Nagaosa and Y. Tokura, Topological properties and dynamics of magnetic skyrmions, *Nat. Nanotech.* **8**, 899 (2013).